Journal of Structural Geology 133 (2020) 104002

Contents lists available at ScienceDirect

Journal of Structural Geology

journal homepage: http://www.elsevier.com/locate/jsg

Hematite fault rock thermochronometry and textures inform fault zone processes

Alexis K. Ault

Department of Geosciences, Utah State University, Logan, UT, 84322, USA

ARTICLE INFO

Keywords:
Hematite
(U–Th)/He thermochronometry
Fault
Textures
Earthquake
Aseismic slip

ABSTRACT

Minerals on fault surfaces record fluid-rock interaction, strain, and/or heat during fault slip. Fault-hosted hematite is amenable to (U–Th)/He (He) thermochronometry. Hematite He dates reflect fault-related processes or exhumation, depending on hematite growth above or below the grain-size controlled closure temperature and processes that promote open system behavior. Deconvolving these phenomena requires multi-scale hematite textural characterization and constraints on the ambient thermal history from conventional thermochronometry. Two examples of this approach include investigations of hematite-coated fault surfaces from exhumed damage zones in the seismically active Wasatch fault zone (WFZ), UT, and Painted Canyon fault (PCF) paralleling the southern San Andreas fault, Mecca Hills, CA. WFZ fault mirrors preserve sub-μm-scale polygonal grain textures and hematite He data patterns that, together with host-rock apatite He data, are consistent with localized friction-generated heat, hematite He loss, and hematite recrystallization during damage zone seismicity <4.5 Ma. In contrast, PCF hematite slip surfaces comprise foliated, nm-thick, high-aspect ratio plates, analogous to scaly clay fabrics, and hematite He dates record syn-kinematic mineralization episodes ~0.7–0.4 Ma via creep processes. These case studies highlight the power of integrated hematite textural observations and targeted fault rock thermochronometry to inform the timing and conditions of seismic to aseismic slip processes.

1. Introduction

Documenting the broad spectrum of fault behavior in space and time anchors efforts to constrain fault mechanics, the rheology of Earth materials, and heat and mass transfer through Earth's crust (Huntington and Klepeis, 2018; Laubach et al., 2019). Faults slip at a range of velocities from creep to episodic slow slip and/or tremor to seismic slip (e.g., Heaton, 1990; Beroza and Mikumo, 1996; Rogers and Dragert, 2003; Obara et al., 2004; Rousset et al., 2019). Deformation over this range of slip rates modifies the thermal, mechanical, and chemical properties of fault rocks (e.g., Sibson, 1981; Caine et al., 1996; Niemeijer et al., 2012; Rowe and Griffith, 2015). Evolving material properties may impact subsequent fault slip rates, deformation mechanisms, and the distribution of deformation in a fault zone (Tenthorey et al., 2003; Savage and Brodsky, 2011; Mitchell et al., 2016; Ault et al., 2019a).

Exhumed fault rocks provide a record of these processes and a platform to connect geophysical, geochemical, and geomechanical observations of deformation (e.g., Rowe and Griffith, 2015, and references therein). Minerals in fault zones record strain, friction-generated heat, fluid circulation, and/or mineralization associated with deformation and are targets for dating fault slip (e.g., Nuriel et al., 2012; Ault et al., 2015). Radioisotopic methods used to directly constrain the timing of brittle fault processes include $^{40}Ar/^{39}Ar$ and K–Ar dating of neo-formed clay in fault gouge (Vrolijk and van der Pluijm, 1999; van der Pluijm et al., 2001; Zwingmann and Mancktelow, 2004; Haines and van der Pluijm, 2008; Duvall et al., 2011; Fitz-Diaz and van der Pluijm, 2013; Scheiber et al., 2019) and pseudotachylytes (Magloughlin et al., 2001; Cosca et al., 2005; Sherlock et al., 2009; Di Vincenzo et al., 2013), as well as U–Pb and U–Th analyses of synkinematic carbonate and opal (Verhaert et al., 2003; Uysal et al., 2007; Watanabe et al., 2008; Nuriel et al., 2011, 2017; 2019; Rittner and Muller, 2011; Roberts and Walker, 2016; Pagel et al., 2018).

Low-temperature thermochronometry of minerals formed in or deformed by faults also offers the potential to document the timing and temperature of brittle fault zone processes. Conventional low-temperature thermochronometry, such as apatite and zircon (U–Th)/He and fission-track dating, quantifies the movement of rocks through the Earth's subsurface owing to the low temperature sensitivity (or closure temperature, T_c, <300 °C) of these systems. Variations in bedrock low-temperature thermochronometry dates and/or

E-mail addresses: alexis.ault@usu.edu, alexis.ault@usu.edu.

https://doi.org/10.1016/j.jsg.2020.104002
Received 1 November 2019; Received in revised form 22 January 2020; Accepted 29 January 2020
Available online 2 February 2020
0191-8141/© 2020 Elsevier Ltd. All rights reserved.

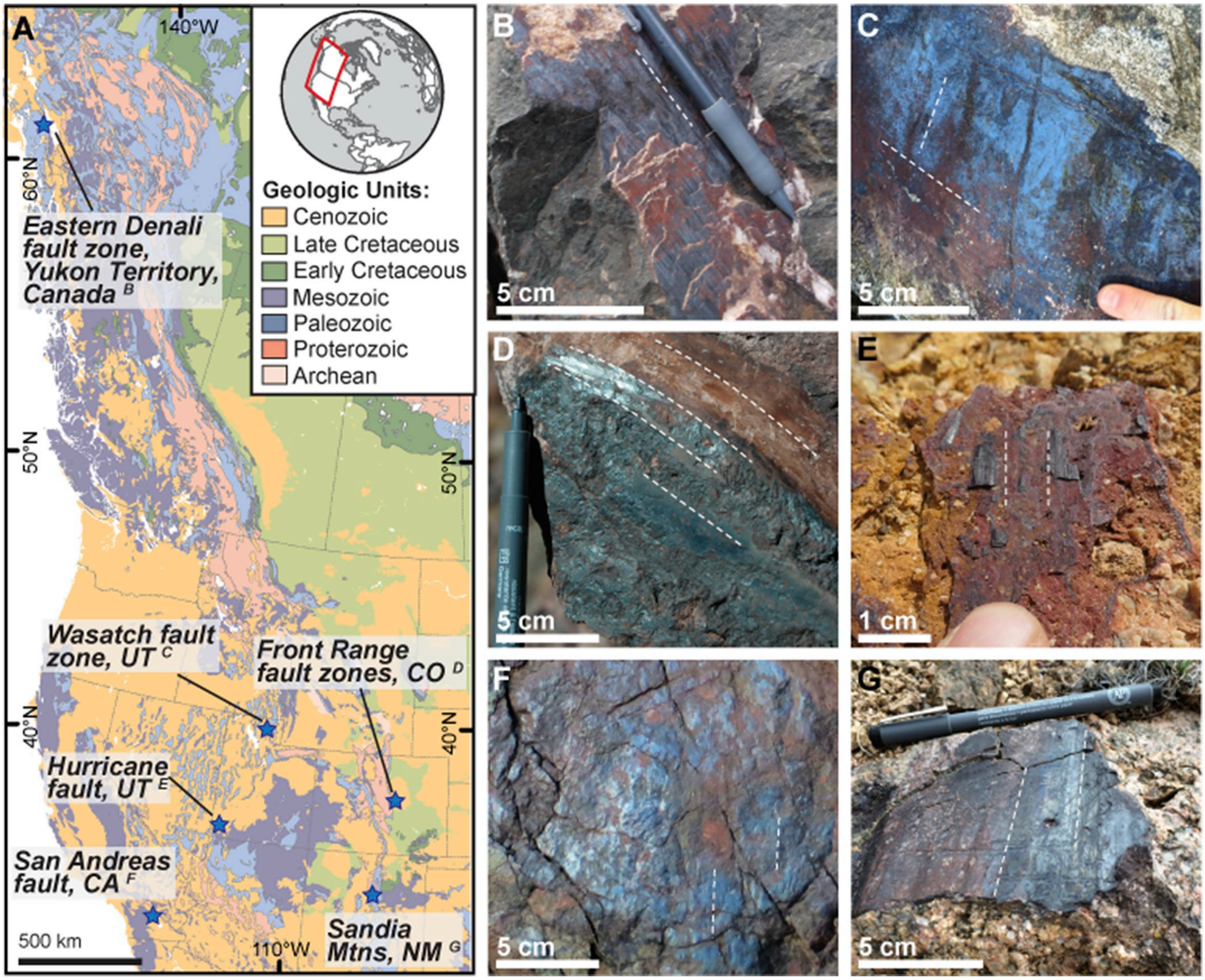

Fig. 1. (A) Simplified geologic map of the North American Cordillera showing locations of hematite-coated fault examples hosted in crystalline basement and sedimentary rocks shown in field photographs, B-G. (B) Striated, metallic hematite slip surface with co-occurring with calcite; eastern Denali fault zone, Yukon Territory, Canada (Caine et al., 2013; McDermott et al., 2019). (C) Hematite fault mirror (FM); southern Brigham city segment, Wasatch fault zone, UT (Evans et al., 2014; Ault et al., 2015; McDermott et al., 2017). (D) Striated, metallic hematite slip surface; Front Range fault zone, Morrison, CO (Ault et al., 2019b). (E) Striated, localized hematite "lens" on bedrock fault scarp; Hurricane fault, La Verkin, UT (Taylor et al., 2019). (F) Striated, metallic hematite slip surface; Painted Canyon fault zone, southernmost San Andreas fault system, Mecca Hills, CA (Moser et al., 2017). (G) Hematite FM; Sandia Mountains, NM (Channer, 2017). Dashed white lines denote slickenline orientation(s).

extrapolated cooling rates can broadly bracket the timing of fault slip (Stockli et al., 2000; Wells et al., 2000; Ehlers and Farley, 2003; d'Alessio and Williams, 2007; Colgan et al., 2008; Bidgoli et al., 2015; Curry et al., 2016; Abbey and Niemi, 2018; Collett et al., 2019; Heineke et al., 2019). These approaches assume that cooling reflects tectonic exhumation, which may not always be the case. Helium diffusion and fission-track annealing also respond to short duration, high temperature thermal pulses associated with frictional heating or hydrothermal fluid circulation in fault zones. For example, shear heating and melting have been detected with zircon (U–Th)/He (zircon He) and zircon fission-track (ZFT) thermochronometry (Murakami and Tagami, 2004; Tagami, 2005, 2012; 2019; Murakami et al., 2006; Tagami and Murakami, 2007; Maino et al., 2015). (U–Th)/He and fission-track thermochronometry also track modern and paleo thermal fluid flow (Tagami and Murakami, 2007; Wolfler et al., 2010; Gorynski et al., 2014; Hickey et al., 2014; Reiners et al., 2014; MacNamee and Stockli, 2015; Ault et al., 2016; Louis et al., 2019; Tagami, 2019).

Hematite is common in fault systems. Hematite precipitates from fluids present in or circulating through fault damage zones and fault cores, forming veins and thin coatings on slip surfaces. Fe-oxides, more broadly, form in a variety of settings in the Earth's upper crust, such as in hydrothermal veins, diagenetic cements in sedimentary rocks, and soil and weathering profiles. Fe-oxides are amenable to (U–Th)/He thermochronometry and this radioisotopic tool has been applied to date hematite, magnetite, and goethite in diverse crustal environments (e.g., Wernicke and Lippolt, 1997; Shuster et al., 2005; Blackburn et al., 2007; Farley and Flowers, 2012; Evenson et al., 2014; Monteiro et al., 2014; Farley and McKeon, 2015; Ault et al., 2016; Cooperdock and Stockli, 2016; Miller et al., 2017; Garcia et al., 2018).

Hematite (U–Th)/He (hematite He) thermochronometry is a powerful tool in fault zones because it offers the potential to not only directly date deformation, but also inform fault slip temperatures, deformation mechanisms, and fault strength, when combined with textural observations. Here I review recent work developing hematite

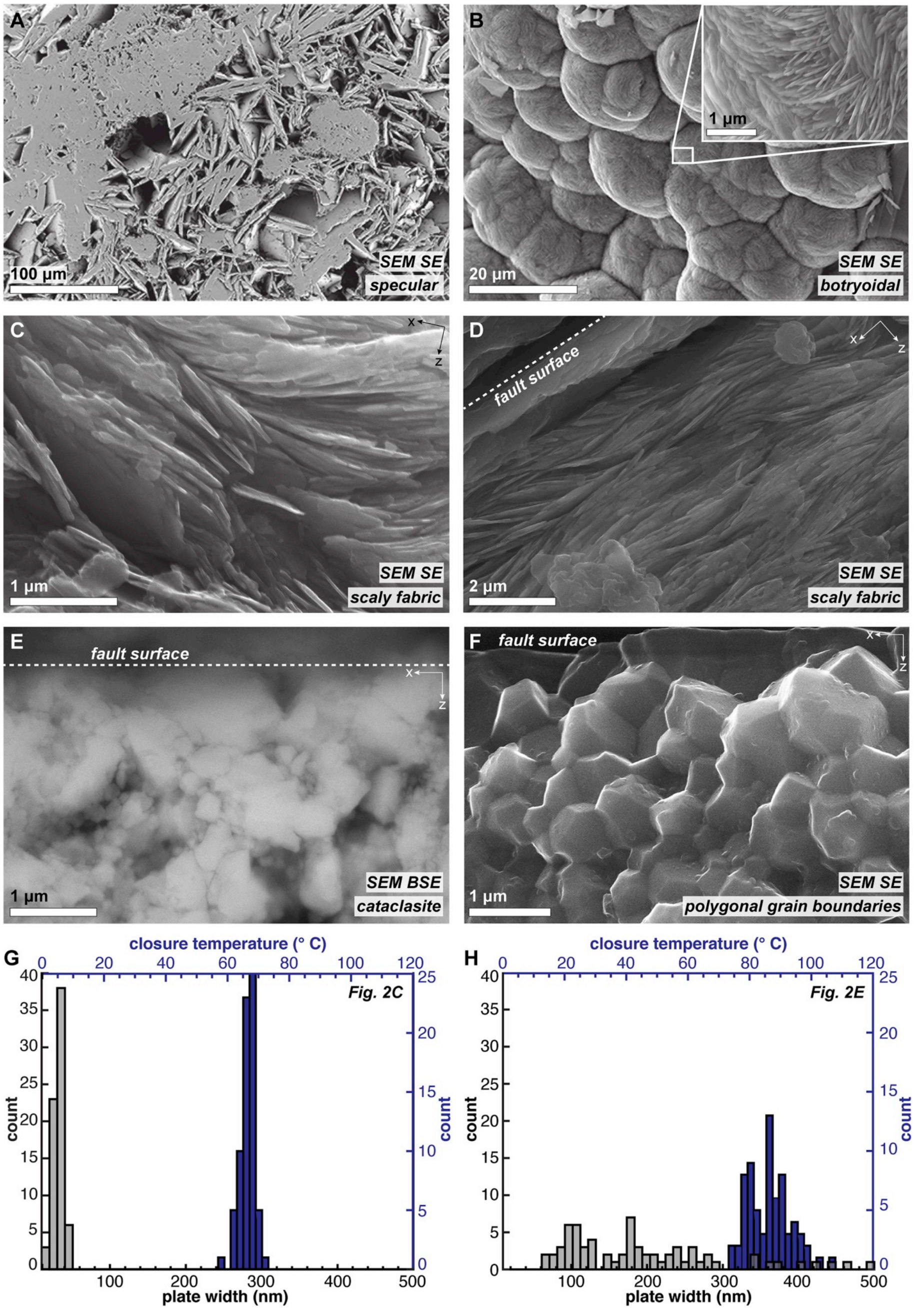

Fig. 2. Scanning electron microscope (SEM) images illustrating diverse fault rock hematite textures and crystal morphologies. (A) Specular and (B) botryoidal hematite from fault-related fissure fills, Gower Peninsula, Wales (Ault et al., 2016). Hematite in foliated, scaly fabrics from (C) Painted Canyon fault, southern San Andreas fault zone, Mecca Hills, CA (Moser et al., 2017) and (D) Kuh-e-Faghan fault, central Iran (Calzolari et al., 2018). (E) Hematite cataclasite from a fault mirror (FM), Wasatch fault zone, UT (McDermott et al., 2017, 2018). (F) Hematite with polygonal grain boundaries from a FM, El Laco Fe-ore deposit, Chile, (Ault et al., 2019a). (G, H) Hematite plate width or particle diameter distribution from C (G) and E (H). Plate half-width or radius converted to closure temperature assuming Farley (2018) diffusion kinetics. SE = secondary electron; BSE = back-scattered electron. x-y-z reference orientation data provided; A-B are unoriented and C–F are in cross-section.

He thermochronometry as applied to fault rocks. I first describe the occurrence, textures, and grain morphologies of hematite in faults, followed by a discussion of hematite He systematics. I discuss approaches to preparing, characterizing, and analyzing hematite for (U–Th)/He dating, as well as potential hematite He data interpretations from fault rocks and strategies for discriminating between possible interpretations. I then provide two examples of an integrated approach combining textural analysis and (U–Th)/He thermochronometry data patterns that reveal two different modes of fault slip in two different fault damage zones: seismic slip on minor faults in the Wasatch fault damage zone, northern UT, and slow slip on small faults in the Painted Canyon fault zone that parallels the southern San Andreas fault in the Mecca Hills, CA.

2. Hematite occurrence and textures in fault rocks

Hematite occurs in some fault cores and as mineral coatings on discrete slip surfaces in some damage zones (Fig. 1). Fault rock hematite exhibits diverse textures and grain morphologies (Fig. 2). These textures reflect the thermal and geochemical conditions, as well as stress state, of hematite growth and post-formation deformation. Hematite precipitates from oxidizing fluids present and circulating in subsurface regions of higher permeability such as faults and fracture networks (e.g., Cornell and Schwertmann, 2003). The subsurface conditions, geochemical reactions, and fluid sources/pathways that control hematite precipitation are beyond the scope of this review. However, I note that hematite formation in fault systems occurs over a range of fluid temperatures and crustal depths (ambient temperatures) from low temperature ($T < 100$ °C) replacive oxides or textural maturation of ferrihydrite to higher temperature ($T \sim 100$–300 °C) mineralization in hydrothermal systems (e.g., Cornell and Schwertmann, 2003; Dideriksen et al., 2007). Hematite can also form from oxidation of pre-existing magnetite, pyrite, or other Fe-bearing phases (e.g., Rosière and Rios, 2004; Loope et al., 2010). Fluid and ambient temperatures and chemistry control, in part, hematite growth texture (specular vs. botryoidal) and grain size (i.e., plate thickness) (Catling and Moore, 2003; Cornell and Schwertmann, 2003).

Hematite in fault veins and breccia cement commonly comprise μm-thick, elongate specular hematite plates (Fig. 2A; e.g., Ault et al., 2016; Jensen et al., 2018). These plates may be preferentially aligned or randomly oriented depending on the stress field and fluid pressure during mineralization (Morales et al., 2008; Rosière et al., 2013). Fault vein hematite can also occur in a dendritic texture with macroscopic botryoidal lobes comprising intricate, radially-oriented plates (Fig. 2B; Ault et al., 2016). Pre-existing hematite may be physically or chemically modified by subsequent deformation via grain-size reduction, recrystallization, and/or fluid-rock interaction. For example, in the Wasatch fault zone, UT, crystalline basement-hosted specular hematite veins are rheologically weak compared to the host rock (i.e., granodiorite). Progressive deformation, grain size reduction, strain localization, and development of thin slip surfaces occur within these specularite veins (Ault et al., 2015; McDermott et al., 2017).

Hematite on thin slip surfaces exhibits a variety of textures. Fault surface fabrics are partially controlled by the grain size distribution and morphology of the original hematite material and/or the conditions of synkinematic mineralization (e.g., Rosière et al., 2013; Moser et al., 2017; Mazzarini et al., 2019). For example, fault surfaces characterized by a metallic, burnished, and undulatory macroscopic appearance (Fig. 1B and 1D) commonly comprise nm-thick, high-aspect ratio hematite plates (Fig. 2C and 2D; Moser et al., 2017). These plates can be randomly oriented, dendritic, or foliated with a shape preferred orientation (SPO) (Calzolari et al., 2018). The foliated hematite texture is similar to scaly fabrics documented in clays in fault zones (Moore et al., 1986; Vannucchi et al., 2003; Schleicher et al., 2010; Chester et al., 2013; Vannucchi, 2019). "Scaly hematite" may deform by individual plates sliding past one another in a distributed network of slip surfaces (cf. Tarling and Rowe, 2016) or by dislocation creep (Ferreira et al., 2016). In contrast, some slip surfaces are characterized by cataclastic hematite comprising subangular to subrounded particles (Fig. 2E). Hematite on these surfaces typically originates as μm-thick, elongate specular plates that fragment and comminute during deformation. Analogous to clays, there may be a plate thickness below which hematite does not comminute during fault slip (Moore and Lockner, 2004).

Fault mirrors (FMs) are a type of thin, localized slip surface. FMs are <1 mm-thick, high-gloss, light-reflective slip surfaces composed of layered nano- to microparticles that can form at seismic to subseismic slip rates (Figs. 1C, G; 2E, 2F; Verberne et al., 2013; Siman-Tov et al., 2015; Pozzi et al., 2018). FMs have been observed in carbonate, quartzite, granite, chert, and hematite (Power and Tullis, 1989; Fondriest et al., 2013; Kirkpatrick et al., 2013; Siman-Tov et al., 2013; Evans et al., 2014; Ault et al., 2015, 2019a; Kuo et al., 2016; McDermott et al., 2017). Nano- and microparticles on hematite FMs exhibit a variety of morphologies from angular cataclastic particles to particles with polygonal (triple-junction-forming; Fig. 2F) or lobate grain boundaries (Ault et al., 2015, 2019a; McDermott et al., 2017). Polygonal hematite grains that lack SPO, crystallographic preferred orientation (CPO), and discrete grain boundaries may reflect grain growth, annealing and/or sintering by thermally-mediated processes (Ault et al., 2019a). The distribution of these particle morphologies relative to the FM surface can inform fault-slip process. For example, polygonal grains that occur in μm-scale clusters may reflect the thermal imprint of paleo-asperities (i.e., asperity flash heating; McDermott et al., 2017). Pervasive polygonal grains and a FM-surface-perpendicular grain size decrease may collectively indicate grain growth following shear heating and associated melting across the FM volume (Ault et al., 2019a).

3. Hematite (U–Th)/He thermochronometry from fault rocks

3.1. Hematite (U–Th)/He systematics

Hematite incorporates U and Th into its crystal lattice at concentrations high enough to be precisely quantified (ppb to 100s of ppm; Wernicke and Lippolt, 1993, 1994a; b, 1997). Analogous to conventional apatite and zircon He dating, hematite He thermochronometry exploits decay of ^{238}U, ^{235}U, and ^{232}Th, associated alpha particle (^{4}He) production, and temperature-dependent ^{4}He diffusion through the crystal lattice (e.g., Strutt, 1909; Zeitler et al., 1987; Wolf et al., 1996; Farley, 2000). Hematite is difficult to date with the U–Pb system due to common Pb issues and is generally too old to date with U-series disequilibrium analysis. However, hematite is suitable for (U–Th)/He analysis because it incorporates negligible initial ^{4}He and retains ^{4}He over geologic timescales.

Prior $^{4}He/^{3}He$ diffusion experiments and numerical calculations applying Density Functional Theory reveal polycrystalline hematite exhibits polydomain diffusion (Farley and Flowers, 2012; Evenson et al., 2014; Farley and McKeon, 2015; Balout et al., 2017). $^{4}He/^{3}He$ analysis quantifies the distribution of ^{4}He in a single crystal or polycrystalline aggregate (e.g., Shuster and Farley, 2004; Shuster et al., 2004; Farley and Flowers, 2012). Stepwise degassing of an aliquot containing synthetic, uniformly distributed, proton-induced ^{3}He constrains the ^{4}He distribution, which is a function of the initial U and Th distribution (Farley et al., 2010) and the thermal history. The hematite ^{3}He Arrhenius relationship yields information about the aliquot's diffusion domain(s) and diffusion kinetics (e.g., Farley and Flowers, 2012; Farley, 2018). Polydomain diffusion from polycrystalline hematite differs from common (U–Th)/He accessory phases such as apatite, zircon, and titanite, which are characterized by a single diffusion domain that is the crystal itself. Polydomain diffusion involves simultaneous He loss from constituent domains (Farley, 2018). Single-crystal hematite He analyses and single-crystal diffusion data from different sized crystals confirm that each hematite crystal in a polycrystalline aggregate is a diffusion domain (Farley, 2018; Jensen et al., 2018). The transition between open to closed system behavior, or He retention, is known as the closure temperature (T_c) (Dodson, 1973). The T_c for the hematite He system is ~25–250 °C, assuming a 10 °C/Myr cooling rate, and T_c increases with increasing grain (domain) size and cooling rate (Farley and Flowers, 2012; Evenson et al., 2014; Jensen et al., 2018). Thus, variations in bulk T_c of a polycrystalline aliquot are controlled by the grain size distribution and the post-formation thermal history.

Hematite He geo- and thermochronometry is a method with historical precedence (Strutt, 1909) and recent applications leverage modern analytical techniques (e.g., Farley and Flowers, 2012). (U–Th)/He thermochronometry has now been successfully applied to Fe-oxides occurring in a variety of settings. For example, hematite He thermochronometry is used to constrain hydrothermal (Wernicke and Lippolt, 1993, 1994a, b, 1997; Lippolt et al., 1995; Farley and Flowers, 2012; Evenson et al., 2014), diagenetic (Reiners et al., 2014), and deformation (Ault et al., 2015; McDermott et al., 2017; Moser et al., 2017; Calzolari et al., 2018) histories. Goethite He and hematite He thermochronometry have been applied to deep weathering horizons (Shuster et al., 2005, 2012; Heim et al., 2006; Vasconcelos et al., 2013; Monteiro et al., 2014, 2018), supergene alteration (Riffel et al., 2016), and petrified wood and soils (Lippolt et al., 1998; Yapp and Shuster, 2011). Magnetite He dating constrains the timing of formation and/or exhumation of intermediate to mafic volcanic rocks (Blackburn et al., 2007) and serpentinites (Cooperdock and Stockli, 2016).

3.2. Fault rock sample preparation, SEM analysis, and (U–Th)/He methods

Hematite is routinely extracted from fault rocks using a rotary tool and/or fine point tweezers. Aliquots are selected avoiding tool marks, so

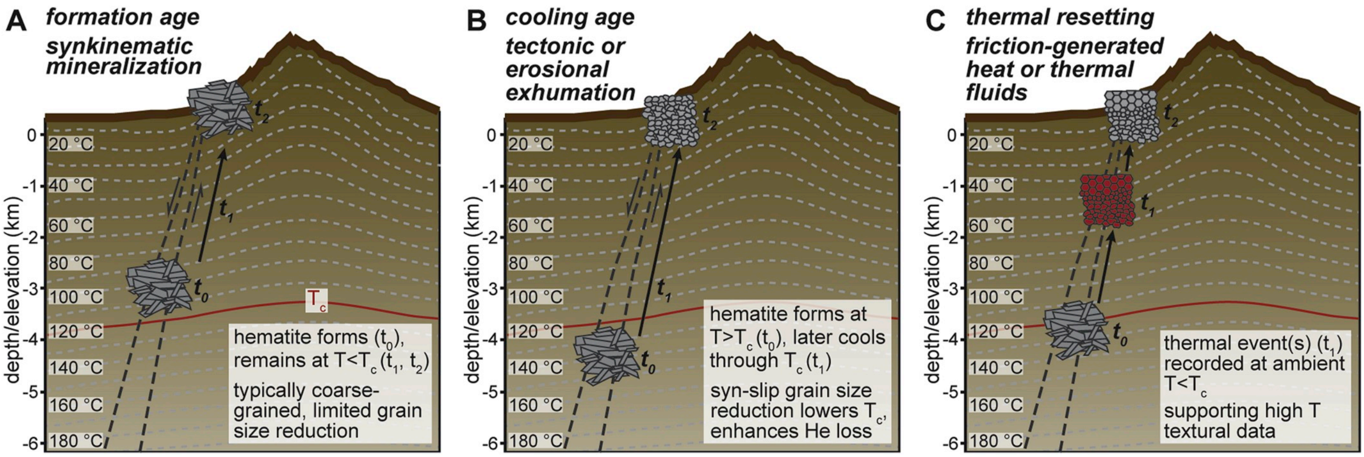

Fig. 3. Potential interpretations of hematite (U–Th)/He (hematite He) thermochronometry data from fault zones. Schematic of a normal fault and hematite aliquot, with hypothetical associated 120 °C closure temperature (T_c). Hematite He dates represents (A) formation age, (B) cooling age, or (C) thermal resetting, depending on the ambient temperature hematite formed relative to T_c, and the post-formation thermal and deformation history.

as not to analyze material that could have experienced He loss associated with sample preparation. Hematite aliquots from fault surfaces are typically polycrystalline aggregates; rectangular, cubic, or irregular in shape; and ~100-200 μm-thick. If a fault vein sample is sufficiently coarse-grained, individual crystals can be isolated using fine-point tweezers (e.g., Jensen et al., 2018). For fault rock analyses, hematite aliquots are commonly selected directly from the fault surface itself. A correction for the fraction of total ^{4}He (FT) lost due to alpha ejection from long alpha stopping distances is usually not applied. This is because alpha ejection is assumed to be balanced by implantation from adjacent hematite crystals. For example, hematite from FMs is sampled directly from the fault surface, as FMs are commonly localized within coarser-grained specular hematite (Ault et al., 2015, 2019a; McDermott et al., 2017). Thus, He ejected from the FM surface is balanced by implantation from He on the opposing side of the FM. Striated, metallic, undulatory fault surfaces may not be localized within hematite and care is required to isolate material that is >20 μm from both the slip surface and the hematite-host rock contact. Aliquots with interstitial phases that are either not He retentive at upper-crustal conditions (e.g., quartz) or rich in U and Th compared to hematite (e.g., zircon, monazite, chrysocolla; Evenson et al., 2014) should be avoided.

Multi-scale scanning electron microscopy (SEM) is required to characterize hematite textures, crystal morphology, and grain size distribution for fault studies. SEM analysis is performed (1) prior to and on the same aliquots targeted for (U–Th)/He thermochronometry (McDermott et al., 2017; Jensen et al., 2018) or (2) on different but representative aliquots in parallel with or after (U–Th)/He analysis (Ault et al., 2015, 2016; Moser et al., 2017; Calzolari et al., 2018). The benefit of the former approach is that thermochronometry dates can be linked to aliquot-specific hematite textures and crystal morphologies as described in the example in section 5.1. If target material is sufficiently coarse-grained and robust, individual plates of specular hematite can be isolated and imaged prior to analysis (Jensen et al., 2018). Polycrystalline or single-crystal aliquots are mounted on Cu- or C-based adhesive tape in cross section. Single plates can also be mounted in plan-view on adhesive tape affixed to a thin metal plate oriented perpendicular to and clamped to the SEM-sample holder. Aliquots are imaged in cross-section under variable pressure or low-vacuum mode. Alternatively, and owing to the fragile and fissile nature of some hematite material, representative hematite aliquots are mounted in cross-section in epoxy, polished, and imaged under high vacuum. In our research group's experience, high-resolution images in excess of 50000x-100000x magnification that capture nano- to microscale hematite textures, grain size, and morphology require a field-emission SEM using epoxy-mounted and polished aliquots. The tradeoff, however, is that these aliquots cannot be used for (U–Th)/He analysis.

Target aliquots for (U–Th)/He thermochronometry are inserted into 1 mm-diameter Nb tubes for He, U, and Th measurement. This includes aliquots affixed to adhesive tape, which are carefully removed without breakage with the aid of ethanol or acetone, to preserve documented textures and grain morphologies. ^{4}He content is determined by laser heating under vacuum and analysis using a noble-gas quadrupole or magnetic sector mass spectrometer. In the Reiners' Arizona Radiogenic Helium Dating Laboratory at the University of Arizona, for example, hematite aliquots are heated to temperatures ~<1000 °C with associated packet "low glow" comparable to temperatures for apatite lasing to prevent U volatilization (e.g., Vasconcelos et al., 2013). Aliquots are commonly heated a second time to temperatures slightly greater than the first extraction or until negligible gas is released. Lasing temperature and time are always sample-specific and generally a function of crystal size. Coarse-grained hematite requires higher lasing temperatures and volatilization can be prevented by extracting ^{4}He *in vacuo* in an O_2-rich atmosphere (Hofmann et al., 2020). Volatilization is monitored by evaluating relationships between intrasample dates and associated Th/U, comparing parent elemental concentrations of degassed and undegassed aliquots from the same sample, and by weighing Nb packets prior to and following lasing. Extracted ^{4}He gas is spiked with ^{3}He and purified using cryogenic and gettering methods. An additional liquid nitrogen cold finger is used to scavenge reactive gas evolved from an aliquot during lasing. Degassed packets are dissolved in hydrochloric or hydrofluoric acid in a pressure digestion vessel (Parr bomb). Following addition of a ^{233}U–^{229}Th spike, equilibration, and dissolution, U and Th isotopes are measured via ICP-MS (Reiners, 2005). Hematite He dates are calculated using the ^{4}He, U, and Th content.

4. Hematite (U–Th)/He thermochronometry data interpretation from faults

4.1. Potential data interpretations

Hematite He thermochronometry dates reflect the conditions of hematite formation and the post-formation thermal, compositional, and mechanical history. This is similar to an apatite He or zircon He date reflecting the samples' chemistry and integrated, potentially non-monotonic, thermal history (e.g., Reiners, 2009; Guenthner et al., 2013; Flowers et al., 2015). An objective of hematite He thermochronometry from fault rocks is to decipher fault-specific processes, such as synkinematic mineralization or thermal resetting due to friction-generated heat, from ambient cooling. In other words, a goal is to differentiate the timing and potentially temperature of fault slip from tectonic

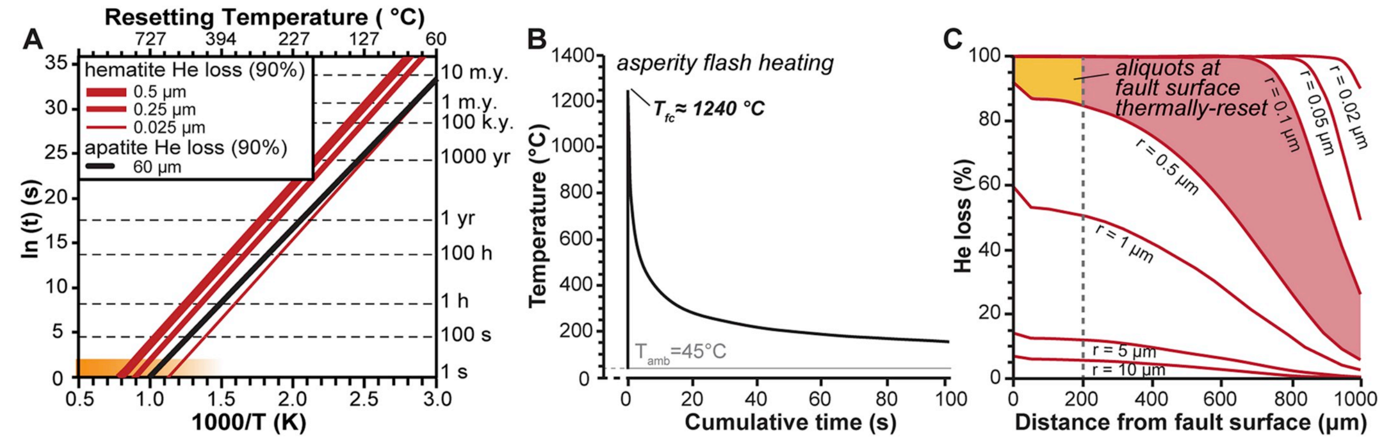

Fig. 4. (A) Temperature (T) and time (t) required to reset the hematite and apatite (U–Th)/He (hematite He, apatite He) systems. Hematite He 90% fractional loss contours as a function of time and inverse of temperature, calculated from a square pulse heating event. He calculations use $E_a = 147.5, 138$ kJ/mol; $D_0 = 3.61E1$, 2.2E-04 cm^2/s (Farley et al., 1996; Evenson et al., 2014); and 0.5, 0.25, 0.025 μm and 60 μm diffusion domain length scales for hematite and apatite, respectively. Orange box denotes coseismic temperatures (Lachenbruch, 1986). Modified from Reiners (2009) and Ault et al. (2015, 2016). (B) Thermomechanical model showing time-temperature history for hematite at fault surface (z = 0 mm) for flash heating at a 20 μm diameter asperity (Lachenbruch, 1986; Rice, 2006). (C) He loss with distance perpendicular to the fault surface for multiple diffusion domains (r) for 20 μm asperity flash heating scenario in B. Red shaded region is bulk He loss for dominant 0.1–0.5 μm grain radii in most fault surface aliquots. Dashed line denotes typical ~200 μm aliquot thickness and yellow shaded region denotes full thermal resetting over dimension typical of most analyzed aliquots. B and C modified from McDermott et al. (2017). (For interpretation of the references to color in this figure legend, the reader is referred to the Web version of this article).

exhumation or erosion. This is challenging for four reasons. First, hematite-coated faults in damage zones or fault cores form or are broadly "active" during exhumation and thus fault-specific and ambient thermal processes may be coeval and/or related. Second, hematite in fault systems, and in general, can form over a range of upper crustal depths and thus ambient temperatures that are above or below its T_c given an initial grain size distribution. Third, aliquots characterized by a range of grain sizes are sensitive to a range of temperatures and may retain a "memory" of their pre-deformation history. Fourth, during fault slip, processes such as cataclasis or pulverization can result in grain size reduction or comminution (Reches and Dewers, 2005; Stünitz et al., 2010). Progressive deformation modifies the diffusion domain length-scale(s) and thus the T_c of an aliquot. Evolution of the diffusion domain distribution presents both challenges and opportunities. On the one hand, decreasing grain size means that hematite aliquots may experience ongoing He loss during exhumation following fault slip, making it more likely that hematite He dates record ambient cooling. On the other hand, smaller diffusion domains are more responsive to short duration, high temperature thermal processes that accompany fault slip.

Hematite He dates from fault zones can be interpreted in several ways (Fig. 3). First, hematite He dates may reflect "formation ages" if the hematite precipitates and remains below (i.e., lower T, shallower depth) its T_c (Fig. 3A; e.g., Farley and McKeon, 2015; Ault et al., 2016; Moser et al., 2017; Jensen et al., 2018). He dates from hematite that mineralizes above (i.e., higher T, greater depths) its nominal T_c may record cooling due to subsequent tectonic or erosional exhumation (Fig. 3B; e.g., Evenson et al., 2014; Calzolari et al., 2018). Finally, hematite on or adjacent to fault surfaces experiences strain, friction-generated heat, and fluid circulation associated with fault slip. Hematite He loss due to reheating from localized fault slip (Ault et al., 2015; McDermott et al., 2017) or thermal fluid circulation (Ault et al., 2016) at ambient conditions lower than its nominal T_c may record the temperatures and timing of these processes (Fig. 3C). Hematite He dates from fault rocks representing synkinematic mineralization or rapid cooling from shear heating or hot fluids directly constrain the timing of a fault-related process. These interpretations, as described below, are bolstered by textural analysis.

The diffusion kinetics of the hematite He system can respond to short duration, high temperature thermal pulses that far exceed the nominal T_c inferred assuming a 10 °C/Myr cooling rate (Ault et al., 2015; McDermott et al., 2017). For these nonmonotonic thermal histories, the temperatures required to induce He loss are inversely proportional to heating duration (Fig. 4A; Reiners, 2009; McDermott et al., 2017). Fig. 4A illustrates thermal resetting and He loss from hematite for different time-temperature histories. Contours of 90% fractional He loss are shown for a square-pulse heating event of different magnitudes and durations for the range of hematite diffusion domain length scales (plate half-width, particle radius). During coseismic slip, temperature rise from work done against friction occurs as bulk fault surface temperature rise or uniform temperature increase on a fault surface (Proctor et al., 2014), shear heating in a deforming layer (Ben-Zion and Sammis, 2013), or asperity flash heating (Archard, 1959; Rice, 2006; Sleep, 2019). The abrupt temperature rise at an asperity contact occurs because heat produced by large contact shear stresses cannot sufficiently diffuse away from the contact during its short lifetime. Thermokinematic models of asperity flash heating for hematite indicate 20 μm-diameter asperities achieve temperatures >1200 °C (Fig. 4B) and induce 90–100% He loss within 200 μm of the fault surface (Fig. 4C) for grain sizes typical of hematite on a fault surfaces (McDermott et al., 2017).

Fault surfaces are dynamic environments that host a cornucopia of thermal, mechanical, chemical, and/or fluid-mediated processes (e.g., Caine et al., 1996; Rowe and Griffith, 2015; Laubach et al., 2019 and many others). These phenomena may induce open-system behavior with respect to parent (U, Th) or daughter (He) components of the (U–Th)/He system, thus impacting hematite He dates. Open-system behavior can yield dispersion at intrasample and/or intersample levels depending on the source of the data varibility. For example, variable U–Th uptake caused by post-formation reaction with fluids (e.g., Reiners et al., 2014) can induce both intrasample and intersample scatter, depending on the variability in the spatial distribution of fluids, fluid chemistry, and the original hematite U–Th concentration. In addition, fault veins and fault surfaces are often polymineralic, owing to heterogeneous fluid chemistry or multiple fluid episodes. Post-mineralization deformation may cause mechanical mixing and introduction of host-rock phases into the deforming volume. In either case, aliquots comprising interstitial phases with different U–Th concentrations and/or He retentivity than surrounding hematite (Evenson et al., 2014) may impact both the parent concentration and the He budget, respectively. Varying portions of these phases in aliquots can yield both intrasample and intersample data dispersion.

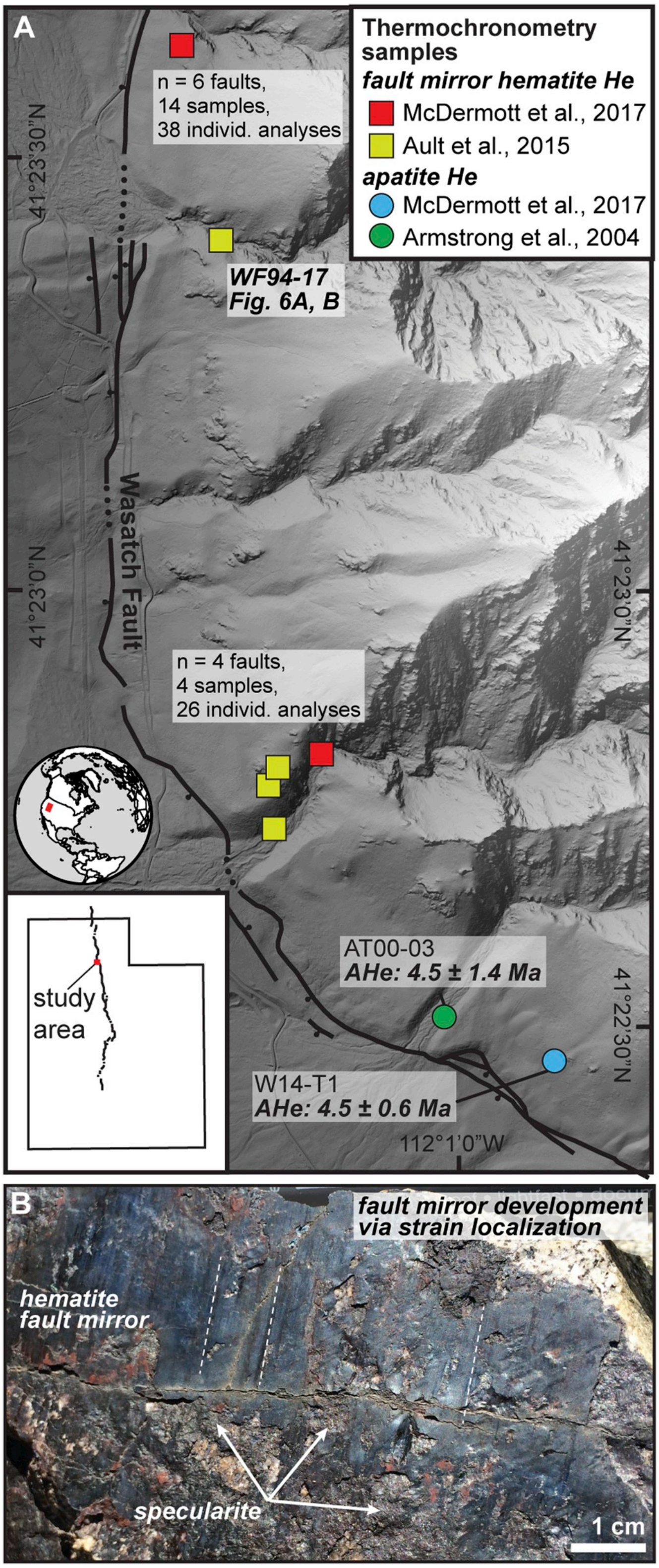

(caption on next column)

Fig. 5. (A) Southern Brigham City segment of the Wasatch fault zone (WFZ) showing location of hematite fault mirrors (FMs) and specularite veins from McDermott et al. (2017; red squares) and Ault et al. (2015; yellow squares) analyzed for hematite (U–Th)/He thermochronometry. Blue (McDermott et al., 2017) and green (Armstrong et al., 2004) circles denote locations of apatite (U–Th)/He thermochronometry data from undeformed and unaltered Farmington Canyon Complex granodiorite. Digital elevation model using 0.5 m LiDAR from the Utah Geological Society with Quaternary fault scarps (black lines) mapped from DEM (McDermott et al., 2017). Insets show location of the study area (red squares). (B) Field photograph showing specular hematite beneath a hematite FM. White dashed lines denote slickenline orientation. (For interpretation of the references to color in this figure legend, the reader is referred to the Web version of this article).

4.2. Strategies for discriminating between different interpretations

Accurate interpretation of hematite He data requires information on hematite aliquot T_c, textural characterization, and constraints on the ambient thermal conditions during and after hematite formation. In addition to characterizing fault surface textures at the nano- to micro-scales and hematite crystal morphology, SEM analysis informs an aliquot's grain size distribution, which is used to bracket the range of potential T_c. SEM data also identifies any post-formation thermo-mechanical alteration or grain size reduction that would reduce the T_c or induce He loss in dated hematite aliquots. Hematite plate thickness or particle diameter are measured to calculate plate half-width or particle radius, respectively. Typically, >50 randomly-selected hematite crystals are measured in an SEM image using Image J, noting the minimum, maximum, mean, and standard deviation of the mean grain sizes. Grain size values are converted into T_c parameters, assuming the correspondence of the physical crystal dimension with the diffusion domain and known diffusion kinetics, such as those derived from single-crystal aliquots reported in Farley (2018). Hematite has an activation energy (E_a) of 171 ± 2.5 kJ/mol and diffusivity at infinite temperature ($\ln(D_0)$) of −0.66 ± 0.35 cm^2/s (Farley, 2018). These values are similar to previously reported E_a and $\ln(D_0)$ of 157 ± 6 kJ/mol and $9.0{*}10^{-5}$ cm^2/s (Farley and Flowers, 2012) and 147.5 kJ/mol and $2.2{*}10^{-4}$ cm^2/s (Evenson et al., 2014). For example, Fig. 2G and 2H presents grain size data and corresponding T_c information from hematite shown in Fig. 2C and 2E, respectively, using Farley (2018) diffusion kinetics. Because SEM images capture the 2-D crystal (domain) structure of a 3-D volume, it is permissible that coarser (higher retentivity) or finer (lower retentivity) hematite crystallites are present in an aliquot, and thus this approach only provides a T_c estimate.

Conventional low-temperature thermochronometry, such as apatite He and apatite fission-track (AFT) data, from nearby and unaltered host-rock informs the ambient thermal history. The apatite He system is sensitive to temperatures of ~90-30 °C, depending on the accumulation of radiation damage in the apatite crystal (Shuster et al., 2006; Flowers et al., 2009; Gautheron et al., 2009; Shuster and Farley, 2009). The T_c of the AFT is ~120-60 °C and varies as a function of apatite chemical composition (Gallagher et al., 1998; Gleadow et al., 2002). For both apatite He and AFT, the magnitude of radiation damage and grain chemistry effects are modulated by the thermal history. Although the potential hematite He T_c range is broad and depends on the grain size distribution, apatite He and AFT thermochronometry data serve as an appropriate benchmark for comparison with the hematite He data owing to the general overlap between the apatite He, AFT, and typical hematite He T_c from fault rocks (e.g., Fig. 2G and 2H). Provided the sample-specific hematite He T_c can be inferred from grain size distribution information, comparison of hematite He with conventional thermochronometry data informs data interpretations. For example, if analyzed hematite has an associated T_c that is similar to or higher than the host-rock apatite He T_c, then hematite He dates older than apatite He dates track cooling due to tectonic or erosional exhumation. Hematite He dates younger than host-rock apatite He dates likely record hematite

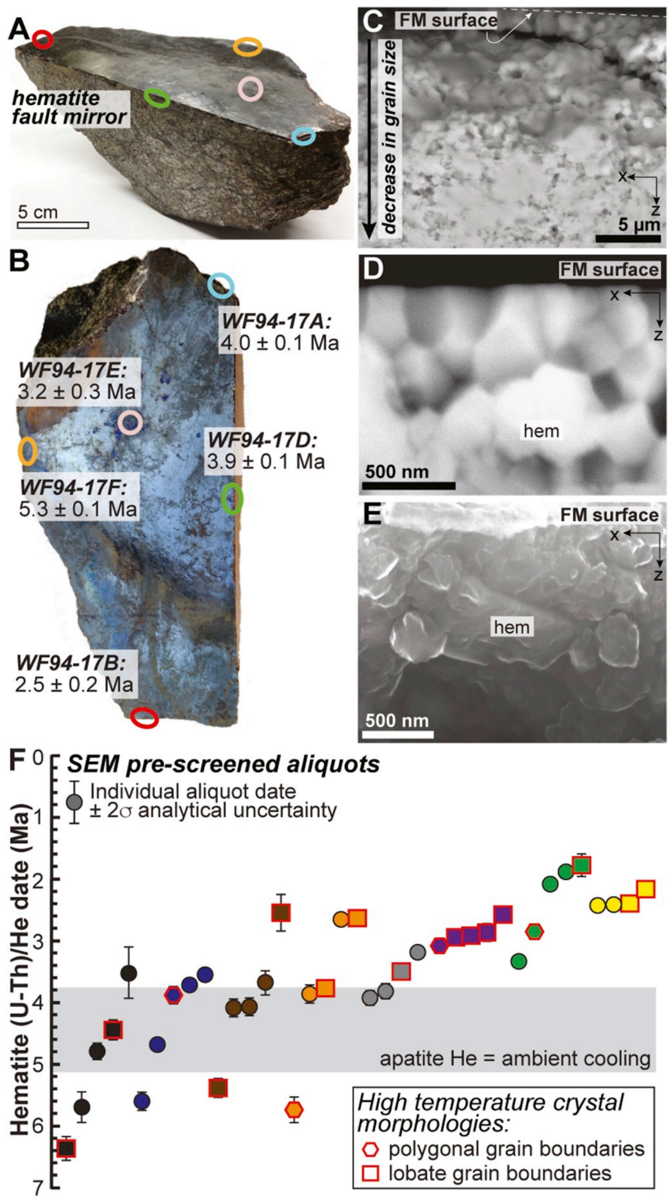

Fig. 6. (A) Oblique cross-sectional and (B) plan view photographs of Wasatch fault zone (WFZ) hematite fault mirror (FM) sample WF94-17 (Ault et al., 2015) showing the location of mean hematite (U–Th)/He (hematite He) thermochronometry dates (±1σ standard deviation). WF94-17A (blue); WF94–17B (red); WF94-17D (green); WF94-17E (pink); WF94–17F (orange). (C–E) Cross-sectional scanning electron microscopy (SEM) secondary electron images showing sub-μm hematite particles with polygonal grain boundaries (C, D; Ault et al., 2015) and lobate grain boundaries (E; McDermott et al., 2017). C shows FM surface-perpendicular decrease in grain size, indicative of a fault perpendicular thermal gradient (cf. Ault et al., 2019a). C acquired from a hematite FM collected in the WFZ by 5th and 6th grade students at the Promontory School for Expeditionary Learning in Perry, UT. x-z reference orientations denoted. (F) Individual hematite He dates (±2σ analytical uncertainty) from SEM-prescreened aliquots classified by sample (different colors) with polygonal (red hexagon outline; C, D) and lobate (red square outline, E) grain boundaries, or inferred high-temperature crystal morphologies. Gray bar is host rock apatite He date (mean ± 1σ standard deviation; Fig. 5A data from McDermott et al., 2017). Aliquots with inferred high-temperature crystal morphologies have hematite He dates younger than benchmark apatite He date requiring enhanced He loss at ambient temperatures lower than the hematite He closure temperature. (For interpretation of the references to color in this figure legend, the reader is referred to the Web version of this article).

formation below its T_c (i.e., formation age) or may record thermal resetting.

In addition, hematite $^4He/^3He$ diffusion experiments characterize He diffusion domains and provide additional constraints on fault-surface thermal histories. Combined with additional geo- and thermochronological (i.e., the bulk (U–Th)/He date) or geologic information, the ^4He concentration profile can be used to more narrowly constrain a sample's thermal history. For example, this tool has also been used to constrain the diffusion kinetics and thermal history of hydrothermal hematite (Farley and Flowers, 2012; Evenson et al., 2014; Farley and McKeon, 2015; Farley, 2018; Garcia et al., 2018), goethite (Shuster et al., 2005; Vasconcelos et al., 2013), and Mn-oxides (Garcia et al., 2018). The shape of the hematite $^4He/^3He$ ratio as a function of cumulative ^3He release (i.e., ratio evolution diagram) can reflect mineralization or thermal resetting from friction-generated heat (plateau), or more protracted tectonic exhumation (curved release pattern). Additional constraints on the thermal and chemical conditions of hematite formation come from fluid inclusion microthermometry of hematite, using an infra-red light, or co-occurring calcite and quartz (Luders, 2016; Jensen et al., 2018).

5. Applications of hematite (U–Th)/He thermochronometry to fault rocks

The power of hematite He thermochronometry from fault rocks is the potential to directly date the timing of brittle deformation and constrain the conditions (i.e., temperature, deformation mechanisms) of fault slip. Accurately interpreting hematite He thermochronometry dates and inferring fault zone processes requires integration of detailed hematite He data with constraints on the host-rock thermal history and multi-scale hematite textural information. Below I provide two examples of this integrated approach, described in section 4.2, to decipher two different modes of fault slip in fault damage zones: seismic slip on minor faults in the Wasatch fault damage zone (WFZ), northern UT and slow slip or creep on small faults subparallel to the southern San Andreas fault (SAF) in Mecca Hills, CA.

5.1. Seismic slip in fault damage zones

A network of hematite FMs in the exhumed, seismogenic WFZ preserve textural and thermochronometric evidence for elevated temperatures during small paleoearthquakes (Ault et al., 2015; McDermott et al., 2017). The WFZ is a seismogenic, segmented normal fault that has experienced earthquakes > M7 in the Holocene (McCalpin and Nishenko, 1996). The southern Brigham City segment of the WFZ comprises a ~300-400 m-wide, ~2 km long footwall damage zone in the Archean and Paleoproterozoic Farmington Canyon Complex gneiss (Fig. 5). Apatite He thermochronometry data indicates the WFZ has been active since ~12 Ma (Ehlers et al., 2003; Armstrong et al., 2004). Hematite FMs are planar to arcuate, locally iridescent, and show <10 cm of observed offset (Fig. 5B; 6A, 6B; Evans et al., 2014). These thin (<2 mm-thick) slip surfaces commonly exhibit one to several sets of slickenlines consistent with normal, down-to-the-west slip, reflecting WFZ extension. Importantly, field and microtextural observations reveal that many now mirrored surfaces originated as specular hematite fault veins that are later modified by progressive slip and associated grain comminution (Fig. 5B; Ault et al., 2015; McDermott et al., 2017). SEM analysis reveals specular veins comprise euhedral to subhedral, elongate hematite plates with ~0.07–10 μm half-widths. FMs locally exhibit comminuted, subrounded to subangular grains with ~0.05–0.5 μm radii, consistent with a cataclastic texture. Some FMs contain ~0.1–0.3 μm-radii crystals with polygonal, triple-junction forming grain boundaries (Fig. 6C and D), and/or lobate grain boundaries (Fig. 6E). Polygonal grains lack a shape preferred orientation (Fig. 6C and D) and occur in spatially-isolated <20 μm clusters at the FM surface surrounded by lobate and/or cataclasite.

Initial field, microtextural, and hematite He thermochronometric data suggested repeated fault slip on hematite FMs (Ault et al., 2015).

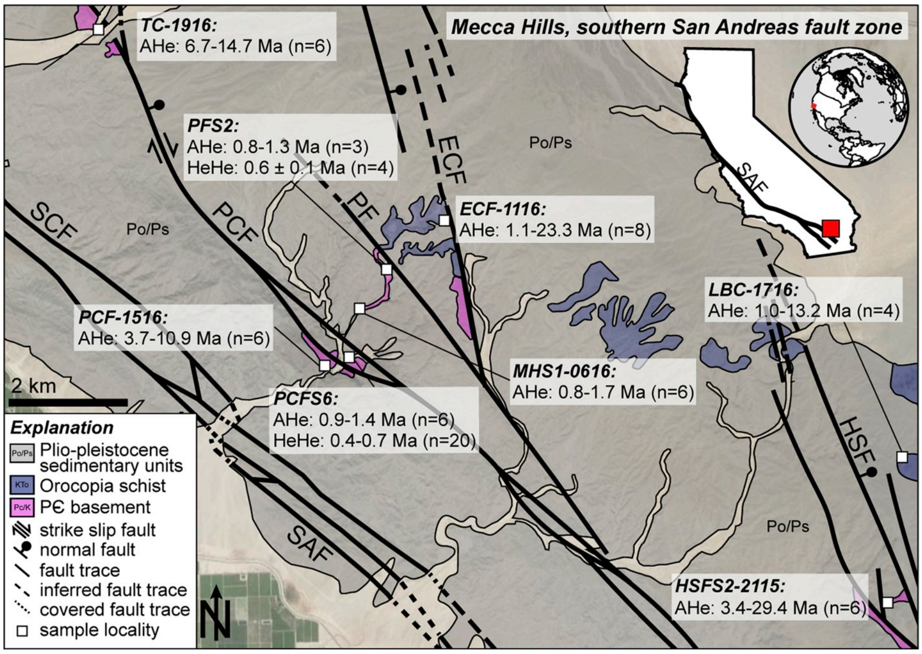

Fig. 7. Mecca Hills, CA, location, geology, and hematite and apatite (U–Th)/He (HeHe, AHe) thermochronometry sample locations and dates. Major faults denoted with black lines, including San Andreas fault (SAF), Skeleton Canyon fault (SCF), Painted Canyon fault (PCF), Platform fault (PF), Eagle Canyon fault (ECF). AHe dates reported as mean ± 1σ standard deviation if % standard deviation < 20% or as range of individual dates if % standard deviation > 20%. PCF hematite He dates reported as range of sample means; PFS2 hematite He date reported as sample mean ± 1σ standard deviation. Insets denote study area location with red squares. Modified from Moser et al. (2017). (For interpretation of the references to color in this figure legend, the reader is referred to the Web version of this article).

Forty-eight individual hematite He dates from 10 samples from five FMs yield mean dates of ~5.7 to ~2.5 Ma, with ~18-7 Ma individual dates from one sample locally comprising specularite plates beneath the FM. Apatite He and AFT dates from the undeformed host rock indicate rapid footwall exhumation ~4.5 Ma. Internally reproducible but disparate sample dates between ~4.5 and 2.5 Ma from isolated locations <10 cm apart on a single FM (Fig. 6A and 6B) do not reflect ambient cooling due to footwall exhumation, which would require extreme variations in geothermal gradient among aliquots with similar grain size distributions and thus T_c. Textural and thermochronometry data patterns are consistent with (1) partial He loss and/or a pre-late Miocene component of the thermal history preserved in some aliquots, (2) footwall exhumation owing to progressive grain size reduction and lowering of the bulk hematite T_c, and (3) localized, friction-generated heat on some FMs.

An expanded hematite He dataset, together with new microtextural analysis and numerical modeling, quantifies fault surface temperatures and reveals a rock record of seismicity on Wasatch FMs (McDermott

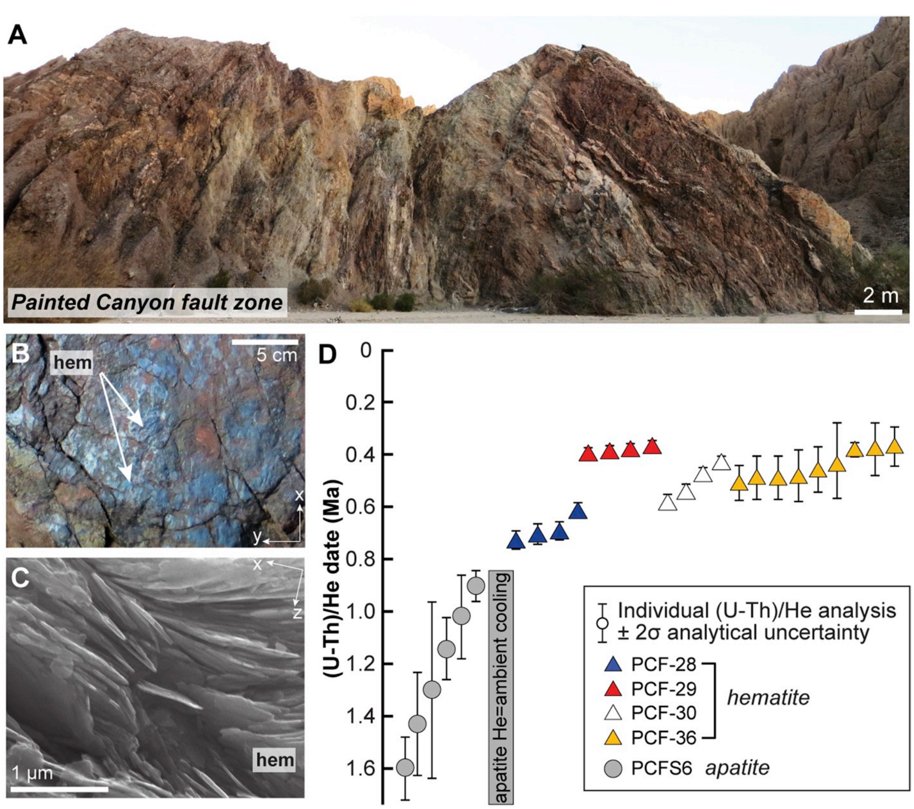

Fig. 8. Field photographs of (A) the Painted Canyon fault zone (PCF) and (B) example of a hematite-coated fault surface in the PCF. (C) Representative, cross-sectional scanning electron microscopy secondary electron image from sample PCF28 with x-z reference orientation shown. (D) Individual apatite and hematite (U–Th)/He dates (±2σ analytical uncertainty) from the PCF zone. Mecca Hills hematite textures from striated fault surfaces (B, C) and hematite He dates younger than apatite He dates reflect synkinematic hematite formation.

et al., 2017). Additional thermochronometry data include n = 66 individual hematite He dates from - seven new fault surfaces and two veins (McDermott et al., 2017). A subset of these hematite aliquots was pre-screened with the SEM prior to (U–Th)/He analysis to link textural development with thermochronometry data patterns (Fig. 6F). Hematite aliquots comprising polygonal and lobate grains at the FM surface, or high temperature microtextures, yield the youngest dates of the pre-screened dataset which are younger than the host rock apatite He dates despite having similar T_c. These collective observations support past, localized, friction-generated heat on the FM interface and associated hematite He thermal resetting.

Most WFZ FMs were repeatedly reactivated, supported by diverse textures on the fault surfaces and multiple slickenline orientations (Evans et al., 2014; Ault et al., 2015; McDermott et al., 2017). Prior slip caused progressive hematite comminution, reduction in the He diffusion domain length scale, and a lower T_c, making the hematite He system susceptible to subsequent thermal resetting by asperity flash heating during fault slip. Thermochronometric evidence for asperity flash heating events <4.5 Ma is preserved at depths lower than the hematite He T_c. Hematite He loss occurs by thermally activated volume diffusion and/or hematite recrystallization, both due to high temperatures generated at frictional contacts. These observations inform thermo-mechanical models of flash heating at frictional contacts and resulting fractional hematite He loss over generated fault surface thermal histories. Temperatures >700–1200 °C, depending on asperity size, are sufficient to induce 85–100% hematite He loss within 200 μm of the fault surface (Fig. 4B and C). Flash heating and associated weakening likely promote earthquake rupture on these minor damage zone fault surfaces. Small earthquakes hosted on the WFZ FM network may represent aftershock clouds occurring at ~2–3 km depth or the upper boundary of the seismogenic zone in this setting (McDermott et al., 2017).

5.2. Slow slip in the rock record

Hematite micro to nano-textures and hematite He thermochronometry from hematite-coated slip surfaces reveal episodes of Pleistocene aseismic fault slip in the Mecca Hills, CA, located adjacent to and northeast of the southernmost SAF system (Figs. 7 and 8; Moser et al., 2017). Active deformation and exhumation in the Mecca Hills reflects transpression on the Coachella section of the SAF (Sylvester and Smith, 1976). Here, a suite of major dextral, oblique normal, and oblique reverse faults subparallel to the SAF cut Plio-Pleistocene sedimentary rocks and underlying crystalline basement (Fig. 7; Dibblee, 1954; Sylvester and Smith, 1976; McNabb et al., 2017). These high-angle structures exhibit shallower dips near the surface and may intersect and merge with a NE-dipping SAF in an inferred flower structure (Sylvester and Smith, 1976; Lindsey and Fialko, 2013; Fattaruso et al., 2014; Fuis et al., 2017; Bergh et al., 2019). Fault zones sub-parallel to the SAF, such as the Painted Canyon fault (PCF) zone, comprise cm-scale clay-rich gouge zones and fault damage zones up to ~1 km wide (Fig. 7; 8A; Sylvester and Smith, 1976; Moser et al., 2017). Damage zones are characterized by a dense network of minor slip surfaces including hematite-coated faults, foliated cataclasite, and delicate clay-coated slip surfaces. Centimeter- to decimeter-scale hematite slip surfaces are metallic, moderately light reflective, and undulatory (Fig. 8B). These surfaces are striated, but lack the iridescent or high-gloss and "polished" appearance characteristic of hematite FMs of the Wasatch fault damage zone (Evans et al., 2014; Ault et al., 2015). Many slip surfaces comprise intercalated hematite with blocky and locally deformed calcite (Moser et al., 2017).

Hematite grain morphology and textures at the micro- to nanoscales from these minor slip surfaces are markedly different from textures observed in the WFZ FMs. In the Mecca Hills, hematite occurs as densely-stacked, foliated, high-aspect ratio hematite plates that form an anastomosing pattern at the microscale (Fig. 8C). Hematite textures and mean hematite plate half-widths are similar within and between samples, ranging from ~14 to 18 nm. These half-widths are correspond to a hematite He T_c of ~60–65 °C, assuming the diffusion kinetics of Evenson et al. (2014). Applying Farley (2018) kinetics yields similar albeit higher values. Hematite plate morphology and foliation is similar to clay scaly fabrics (e.g., Vannucchi, 2019). Scaly hematite fabrics are documented on small faults in the Kuh-e-Faghan strike-slip fault system, central Iran from punctuated Miocene mineralization during fault-related exhumation (Fig. 2D; Calzolari et al., 2018).

Individual hematite He dates from 24 aliquots from 5 discrete slip surfaces in the PCF and Platform fault damage zones yield reproducible dates from the same slip surfaces, but disparate dates between slip surfaces (Fig. 7; Moser et al., 2017). In the PCF, for example, mean sample dates range from ~0.7–0.4 Ma and are younger than ~1.2 Ma apatite He dates from adjacent crystalline basement host rock (Fig. 8D). Given the similarity in T_c between the hematite and apatite He systems, if the hematite formed at depths greater than its T_c and cooled through these temperatures, then the hematite and apatite He dates should overlap (i.e., the hematite He dates record exhumation). However, textural and temporal data patterns require that the hematite formed at depths equivalent to and/or shallower than the hematite/apatite T_c and remained below those temperatures since formation ~0.7–0.4 Ma. A broader apatite He thermochronometry dataset and date-eU patterns from gneissic and Orocopia Schist basement exposed in drainages across Mecca Hills are consistent with variable thermal histories in different fault blocks (Fig. 7; Moser et al., 2017).

Hematite textures coupled with thermochronometry inform deformation mechanisms and fault slip rates operative on minor faults in voluminous damage zones in the Mecca Hills. Thermochronometry data patterns and hematite nano- to microtextures are consistent with Late Pleistocene episodes of synchronous fault slip, fluid flow, and syn-kinematic hematite mineralization in damage zones away from the main trace of the SAF (Moser et al., 2017). Scaly clay fabrics can be associated with multiple modes of fault slip from creep to tremor and seismic slip (e.g., Vannucchi, 2019). Thus, hematite occurrence as high aspect-ratio, foliated plates analogous to clay textures alone is not sufficient to inform slip rate on Mecca Hills hematite fault surfaces. Seismic slip can induce differential He loss by thermal and mechanical processes (Ault et al., 2015; McDermott et al., 2017), which yields dispersed intrasample hematite He dates. Reproducible intrasample hematite He dates suggest PCF surfaces were not significantly heated during fault slip (Moser et al., 2017). Mecca Hills foliated hematite are also associated with calcite that exhibits crack-seal textures. The combination of these observations implies deformation on PCF slip surfaces was accommodated by alternating crack-seal processes, related to fluid pressurization or seismicity, and aseismic hematite mineralization and potentially on-going slip during the interseismic period (Moser et al., 2017). Creep may have occurred via a network of distributed slip surfaces defined by hematite grain boundaries and aligned plates in an anastomosing, shingled pattern, similar to observations from analog modeling (Tarling and Rowe, 2016). Hematite textures and grain morphologies described in the Mecca Hills example are characteristic of hematite observed in many small faults in upper crustal fault zones in the North American Cordillera, which are the subject of on-going research in our group (e.g., Ault et al., 2019b; McDermott et al., 2019). The prevalence of these textures suggests it is characteristic of hematite occurrence and deformation mechanisms in the upper 2 km of the crust.

6. Challenges and opportunities

Thermal, chemical, mechanical, and fluid-mediated processes operative in fault systems present challenges and opportunities for interpreting hematite He thermochronometry data from fault rocks. These phenomena, combined with the polycrystalline nature and polydomain He diffusion behavior of most target aliquots, as well as the potential for an evolving He diffusion domain distribution, can induce open system

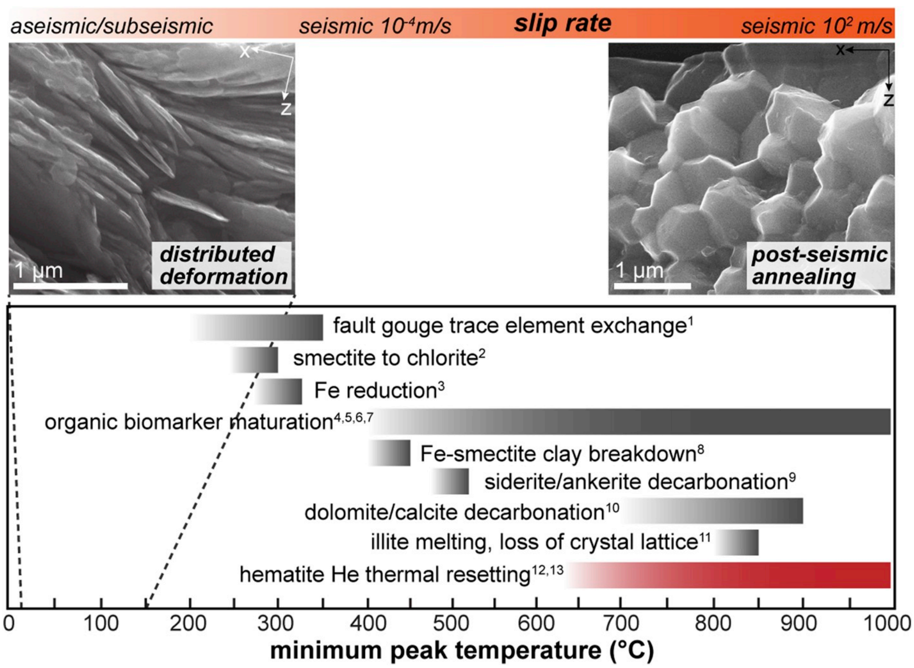

Fig. 9. Hematite textures, illustrated with cross-sectional scanning electron microscope images (with x-z reference orientations), suggestive of different fault slip rates and temperatures (top orange bar). Frictional heating temperature proxies for minimum peak temperatures in fault and earthquake studies broadly associated with rates in top orange bar. All proxies shown in gray are based on heating rates on the order of 10s–100 s °C/m. Data from [1]Ishikawa et al. (2008), [2]Kameda et al. (2011), [3]Evans et al. (2014), [4]Savage et al. (2014) [5] Sheppard et al. (2015), [6]Rabinowitz et al. (2017), [7]Savage and Polissar (2019), [8]Collettini et al. (2013), [9]Isambert et al. (2003),[10]McIntosh et al. (1990), [11]Grim and Bradley (1940), [12]Ault et al. (2015), [13]McDermott et al. (2017) (Grim and Bradley, 1940; McIntosh et al., 1990; Isambert et al., 2003; Ishikawa et al., 2008; Kameda et al., 2011). (For interpretation of the references to color in this figure legend, the reader is referred to the Web version of this article).

behavior that complicates straightforward interpretation of hematite fault rock thermochronometry data. In addition, fault reactivation and fluid-circulation in these systems may occur long after fault formation (Ault et al., 2016). For these reasons, hematite He thermochronometry data from fault rocks cannot be interpreted without key supporting information. Data interpretation requires assessment of intrasample and intersample hematite He data patterns, together with SEM-based textural, grain morphology, and grain size information integrated with conventional thermochronometry data from adjacent host rocks. The combination of these data permits not only accurate interpretation of hematite He results, but also informs fault zone processes through time.

Hematite exhibits potentially diagnostic grain morphologies and fault surface textures that can inform fault rheology and slip mechanics (Fig. 9). For example, foliated, nm-scale-thick, high-aspect ratio hematite plates, analogous to scaly fabrics in clays (e.g., Vannucchi, 2019), may accommodate deformation by slow slip or creep. Whether deformation and fabric development occur via interplate slip or dislocation creep is unclear. Hematite deformation experiments at slow slip rates coupled with multi-scale microscopy have the potential to shed light on deformation mechanisms. In contrast, polygonal grains and/or sintered nanoparticles imply friction-generated heat at coseismic slip rates. Significantly elevated temperatures are required to fuse, recrystallize, or regrow hematite grains. SPO and CPO data, acquired by SEM electron back-scattered diffraction (Ault et al., 2019a), can inform the stress and thermal conditions of deformation reflected in preserved textures. The temperature evolution of thin, localized slip surfaces is linked to rheological changes that control fault strength during the earthquake cycle. For example, the growth of nano- to microscale polygonal grains during post-seismic thermal decay (Fig. 9) likely promotes re-strengthening of material in the deforming zone (Ault et al., 2019a). This has implications for strain delocalization and activation of different fault surfaces in a damage zone through time.

Hematite He data patterns provide additional insight into fault zone processes. For example, it is permissible that foliated hematite (Fig. 9) may develop over a range of slip rates similar to clays (Vannucchi, 2019), but uniform intrasample hematite He dates from these textures suggest on-going deformation does not induce appreciable He loss via thermal or mechanical processes supporting low slip rates. At the other end of the slip rate spectrum, friction-generated heat imparts distinct hematite He data patterns and this tool can be used as a fault slip thermometer. Earthquake energy budgets estimate ~90% of work done against friction dissipates as heat (McGarr, 1999; Scholz, 2002; Kanamori and Riviera, 2006). Hematite He diffusion kinetics respond to transient coseismic thermal pulses (Reiners, 2009; Ault et al., 2015; McDermott et al., 2017). This tool adds to a growing suite of approaches that are used to detect thermal fingerprints of past earthquakes (Fig. 9) in exhumed fault rocks. Coupling high-spatial resolution hematite He data with temperature-induced textures can map out the distribution of heat on a thin slip surface. On-going and future work seeks to isolate and date individual asperities or other μm-scale textural components of a fault surface to fingerprint deformation events. This requires measuring associated U, Th, and He quantities that push current instrumentation detection limits. In addition, integration of textural observations from other minerals provides complementary insight into slip rates, fault surface temperatures, and fluid temperatures and chemistries. Collectively, these fault rock observations provide a critical window into the local and regional conditions of deformation in a fault zone.

Declaration of competing interest

The authors declare that they have no known competing financial interests or personal relationships that could have appeared to influence the work reported in this paper.

Acknowledgements

This contribution would not be possible without the hard work and tenacity of USU graduate and undergraduate students and postdoctoral fellows in my research group. In particular, Robert McDermott, Amy Moser, Gabriele Calzolari, Jordan Jensen, Madison Taylor, and Kelsey Wetzel have been instrumental in pushing the boundaries of applying hematite (U–Th)/He thermochronometry to natural and experimental fault rocks. I am grateful for on-going collaborations with colleagues Pete Reiners (UA), who inspires me with his creativity and continues to challenge me to think outside the box; Jonathan Caine (USGS), whose fault expertise and camaraderie has been invaluable; and Jim Evans (USU), whose foundational fault mirror observations and on-going insights guided some of this work. I thank Fen-Ann Shen (USU) and Uttam

Chowdhury (UA) for analytical support. I thank editor Stephen Laubach and two anonymous reviewers for edits that improved the clarity of the manuscript. I thank Margo Odlum (USU), Amy Moser (UCSB), Jordan Jensen (Exxon), and Alex DiMonte (USU) for feedback on an earlier version of the manuscript and figures. This work is supported by the National Science Foundation CAREER EAR-1654628 (Ault), NSF EAR-1419828 (Ault, Reiners, Evans, Shuster), and NSF PF-1144905 (Ault) and Southern California Earthquake Center grants 17164 (Ault) and 14125 (Evans and Ault).

References

Abbey, A.L., Niemi, N.A., 2018. Low-temperature thermochronometric constraints on fault initiation and growth in the northern Rio Grande rift, upper Arkansas River valley, Colorado, USA. Geology 46, 627–630.

Archard, J.F., 1959. The temperature of rubbing surfaces. Wear 2, 438–455.

Armstrong, P.A., Taylor, A.R., Ehlers, T.A., 2004. Is the Wasatch fault footwall (Utah, United States) segmented over million-year time scales? Geology 32, 385–388.

Ault, A.K., Frenzel, M., Reiners, P.W., Woodcock, N.H., Thomson, S.N., 2016. Record of paleofluid circulation in faults revealed by hematite (U-Th)/He and apatite fission-track dating: an example from Gower Peninsula fault fissures, Wales. Lithosphere 8, 379–385.

Ault, A.K., Jensen, J.L., McDermott, R.G., Shen, F.-A., Van Devener, B.R., 2019a. Nanoscale evidence for temperature-induced transient rheology and postseismic fault healing. Geology 47, 1203–1207.

Ault, A.K., Reiners, P.W., Evans, J.P., Thomson, S.N., 2015. Linking hematite (U-Th)/He dating with the microtextural record of seismicity in the Wasatch fault damage zone, Utah, USA. Geology 43, 771–774.

Ault, A.K., Reiners, P.W., Geissman, J.W., Taylor, M.P., 2019b. Hematite (U-Th)/He thermochronometry constraints on fault surface processes and open system (He) behavior: an example from the Front Range, Morrison, CO. Geol. Soc. Am. Abstr. Progr. 51 (5). Phoenix, AZ, September 2019.

Balout, H., Roques, J., Gautheron, C., Tassan-Got, L., Mbongo-Djimbi, D., 2017. Helium diffusion in pure hematite (α-Fe2O3) for thermochronometric applications: a theoretical multi-scale study. Comput. Theor. Chem. 1099, 21–28.

Ben-Zion, Y., Sammis, C.G., 2013. Shear heating during distributed fracturing and pulverization of rocks. Geology 41, 139–142.

Bergh, S.G., Sylvester, A.G., Damte, A., Indrevær, K., 2019. Polyphase kinematic history of transpression along the Mecca Hills segment of the San Andreas fault, southern California. Geosphere 15, 901–934.

Beroza, G.C., Mikumo, T., 1996. Short slip duration in dynamic rupture in the presence of heterogeneous fault properties. J. Geophys. Res.: Solid Earth 101, 22449–22460.

Bidgoli, T.S., Stockli, D.F., Walker, J.D., 2015. Low-temperature thermochronologic constraints on the kinematic histories of the Castle Cliffs, Tule Springs, and Mormon Peak detachments, southwestern Utah and southeastern Nevada. Geosphere 11, 850–867.

Blackburn, T.J., Stockli, D.F., Walker, J.D., 2007. Magnetite (U-Th)/He dating and its application to the geochronology of intermediate to mafic volcanic rocks. Earth Planet Sci. Lett. 259, 360–371.

Caine, J.S., Evans, J.P., Forster, C.B., 1996. Fault zone architecture and permeability structure. Geology 24, 1025–1028.

Caine, J.S., Israel, S.A., Sicard, K.R., Hults, C.P., 2013. Denali damage: bedrock deformation, kinematics, and fluid flow in the brittle regime along the Denali fault zone, Kluane Lake, Yukon Territory, Canada. Geol. Soc. Am. Abstr. Progr. 45, 749.

Calzolari, G., Rossetti, F., Ault, A.K., Lucci, F., Olivetti, V., Nozaem, R., 2018. Hematite (U-Th)/He thermochronometry constrains strike-slip faulting on the Kuh-e-Faghan fault, central Iran. Tectonophysics 728–729, 41–54.

Catling, D.C., Moore, J.M., 2003. The nature of coarse-grained crystalline hematite and its implication for the early environment of Mars. Icarus 165, 277–300.

Channer, M.A., 2017. (U-Th)/He Thermochronologic Constraints on Secondary Iron-Oxide Mineralization in Southwestern. New Mexico [All Graduate Theses and Dissertations thesis]. Utah State University, Logan, UT.

Chester, F.M., Rowe, C.D., Ujiie, K., Kirkpatrick, J.D., Regalla, C., Remitti, F., Moore, J. C., Toy, V., Wolfson-Schwehr, M., Bose, S., 2013. Structure and composition of the plate-boundary slip zone for the 2011 Tohoku-Oki earthquake. Science 342, 1208–1211.

Colgan, J.P., Shuster, D.L., Reiners, P.W., 2008. Two-phase Neogene extension in the northwestern Basin and Range recorded in a single thermochronology sample. Geology 36, 631–634.

Collett, C.M., Duvall, A.R., Flowers, R.M., Tucker, G.E., Upton, P., 2019. The timing and style of oblique deformation within New Zealand's Kaikōura Ranges and Marlborough Fault System based on low-temperature thermochronology. Tectonics 38, 1250–1272.

Collettini, C., Viti, C., Tesei, T., Mollo, S., 2013. Thermal decomposition along natural carbonate faults during earthquakes. Geology 41, 927–930.

Cooperdock, E.H., Stockli, D.F., 2016. Unraveling alterations histories in serpentinites and associated ultramafic rocks with magnetite (U-Th)/He geochronology. Geology 44, 967–970.

Cornell, R.M., Schwertmann, U., 2003. The Iron Oxides: Structure, Properties, Reactions, Occurrences and Uses. John Wiley & Sons, p. 664.

Cosca, M.A., Caby, P., Bussya, F., 2005. Geochemistry and $^{40}Ar/^{39}Ar$ geochronology of pseudotachylite associated with UHP whiteschists from the Dora Maira massif, Italy. Tectonophysics 402, 93–110.

Curry, M.A.E., Barnes, J.B., Colgan, J.P., 2016. Testing fault growth models with low-temperature thermochronology in the northwest Basin and Range, USA. Tectonics 35, 2467–2492.

d'Alessio, M.A., Williams, C.F., 2007. Putting it all together: exhumation histories from a formal combination of heat flow and a suite of thermochronometers. J. Geophys. Res. 112.

Di Vincenzo, G., Rossetti, F., Viti, C., Balsamo, F., 2013. Constraining the timing of fault reactivation: eocene coseismic slip along a Late Ordovician ductile shear zone (northern Victoria Land, Antarctica). Geol. Soc. Am. Bull. 125, 609–624.

Dibblee, T.W., 1954. Geology of the imperial valley region, California. Geol. South. Calif. Bull. Galif. Div. Mines Geol. 170, 21–28.

Dideriksen, K., Christiansen, B.C., Baker, J.A., Frandsen, C., Balic-Zunic, T., Tullborg, E., Mørup, S., Stipp, S.L.S., 2007. Fe-oxide fracture fillings as a palæo-redox indicator: structure, crystal form and Fe isotope composition. Chem. Geol. 244, 330–343.

Dodson, M.H., 1973. Closure temperatures in cooling geological and petrological systems. Contrib. Mineral. Petrol. 40, 259–274.

Duvall, A.R., Clark, M.K., van der Pluijm, B.A., Li, C., 2011. Direct dating of Eocene reverse faulting in northeastern Tibet using Ar-dating of fault clays and low-temperature thermochronometry. Earth Planet Sci. Lett. 304, 520–526.

Ehlers, T.A., Farley, K.A., 2003. Apatite (U-Th)/He thermochronometry: methods and applications to problems in tectonics and surface processes. Earth Planet Sci. Lett. 206, 1–14.

Ehlers, T.A., Willett, S.D., Armstrong, P.A., Chapman, D.S., 2003. Exhumation of the central Wasatch Mountains, Utah: 2. Thermokinematics of exhumation, erosion, and thermochronometer interpretation. J. Geophys. Res. 108, 2173.

Evans, J.P., Prante, M.R., Janecke, S.U., Ault, A.K., Newell, D.N., 2014. Hot faults: iridescent slip surfaces with metallic luster document high-temperature ancient seismicity in the Wasatch fault zone. Geology 42, 636-626.

Evenson, N.S., Reiners, P.W., Spencer, J., Shuster, D.L., 2014. Hematite and Mn oxide (U-Th)/He dates from the Buckskin-Rawhide detachment system, western Arizona: constraining the timing of mineralization and hematite (U-Th)/He systematics. Am. J. Sci. 314, 1373–1435.

Farley, K.A., 2000. Helium diffusion from apatite: general behavior as illustrated by Durango fluorapatite. J. Geophys. Res. 105, 2903–2914.

Farley, K.A., 2018. Helium diffusion parameters of hematite from a single-diffusion-domain crystal. Geochem. Cosmochim. Acta 231, 117–129.

Farley, K.A., Flowers, R.M., 2012. U-Th)/Ne and multidomain (U-Th)/He systematics of a hydrothermal hematite from eastern Grand Canyon. Earth Planet Sci. Lett. 359–360, 131–140.

Farley, K.A., McKeon, R.E., 2015. Radiometic dating and temperature history of banded iron formation-associated hematite, Gogebic iron range, Michigan, USA. Geology 43, 1083–1086.

Farley, K.A., Shuster, D.L., Watson, E.B., Wanser, K., Balco, G., 2010. Numerical investigations of apatite $^{4}He/^{3}He$ thermochronometry. G-cubed 11. Art. No. Q10001.

Farley, K.A., Wolf, L.T., Silver, L.T., 1996. The effects of long alpha-stopping distances on (U-Th)/He ages. Geochem. Cosmochim. Acta 60, 4223–4229.

Fattaruso, L.A., Cooke, M.L., Dorsey, R.J., 2014. Sensitivity of uplift patterns to dip of the san Andreas fault in the Coachella valley, California. Geosphere 10, 1235–1246.

Ferreira, F., Lagoeiro, L.E., Morales, L.F.G., de Oliveira, C.G., Barbosa, P.F., Ávila, C., Cavalcante, G.C.G., 2016. Texture development during progressive deformation of hematite aggregates: constraints from VPSC models and naturally deformed iron oxides from Minas Gerais, Brazil. J. Struct. Geol. 90, 111–127.

Fitz-Diaz, E., van der Pluijm, B.A., 2013. Fold dating: a new Ar/Ar illite dating application to constrain the age of deformation in shallow crustal rocks. J. Struct. Geol. 54, 174–179.

Flowers, R.M., Farley, K.A., Ketcham, R.A., 2015. A reporting protocol for thermochronologic modeling illustrated with data from the Grand Canyon. Earth Planet Sci. Lett. 432, 425–435.

Flowers, R.M., Ketcham, R.A., Shuster, D.L., Farley, K.A., 2009. Apatite (U-Th)/He thermochronometry using a radiation damage accumulation and annealing model. Geochem. Cosmochim. Acta 73, 2347–2365.

Fondriest, M., Smith, S.A.F., Candela, T., Nielsen, S.B., Mair, K., Di Toro, G., 2013. Mirror-like faults and power dissipation during earthquakes. Geology 41, 1175–1178.

Fuis, G.S., Bauer, K., Goldman, M.R., Ryberg, R., Langenheim, V.E., Scheirer, D.S., Rymer, M.J., Stock, J.M., Hole, J.A., Catchings, R.D., 2017. Subsurface geometry of the san Andreas fault in southern California: results from the Salton seismic imaging project (SSIP) and strong ground motion expectations. Bull. Seismol. Soc. Am. 107, 1642–1662.

Gallagher, K., Brown, R.W., Johnson, C., 1998. Fission track analysis and its application to geological problems. Annu. Rev. Earth Planet Sci. 26, 519–572.

Garcia, V.H., Reiners, P.W., Shuster, D.L., Idleman, B.D., Zeitler, P.K., 2018. Thermochronology of sandstone-hosted secondary Fe- and Mn-oxides near Moab, Utah: record of paleo-fluid flow along a fault. Geol. Soc. Am. Bull. 130, 93–113.

Gautheron, C., Tassan-Got, L., Barbarand, J., Pagel, M., 2009. Effect of alpha-damage annealing on apatite (U-Th)/He thermochronology. Chem. Geol. 266, 157–170.

Gleadow, A.J.W., Belton, D.X., Kohn, B.P., Brown, R.W., 2002. Fission track dating of phosphate minerals and the thermochronology of apatite. Rev. Mineral. Geochem. 48, 579–630.

Gorynski, K.E., Walker, J.D., Stockli, D.F., Sabin, A., 2014. Apatite (U–Th)/He thermochronometry as an innovative geothermal exploration tool: a case study from the southern Wassuk Range, Nevada. J. Volcanol. Geoth. Res. 270, 99–114.

Grim, R.E., Bradley, W.F., 1940. Investigation of the effect of heat on the clay minerals illite and montmorillonite. J. Am. Ceram. Soc. 23, 242–248.
Guenthner, W.R., Reiners, P.W., Ketcham, R.A., Nasdala, L., Giester, G., 2013. Helium diffusion in natural zircon: radiation damage, anisotropy, and the interpretation of zircon (U-Th)/He thermochronology. Am. J. Sci. 313, 145–198.
Haines, S.H., van der Pluijm, B.A., 2008. Clay quantification and Ar-Ar dating of synthetic and natural gouge: application to the Miocene Sierra Mazatan detachment fault, Sonora, Mexico. J. Struct. Geol. 30, 525–538.
Heaton, T.H., 1990. Evidence for and implications of self-healing pulses of slip in earthquake rupture. Phys. Earth Planet. In. 64, 1–20.
Heim, J.A., Vasconcelos, P.M., Shuster, D.L., Farley, K.A., Broadbent, G., 2006. Dating paleochannel iron ore by (U-Th)/He analysis of supergene goethite, Hamersley province, Australia. Geology 34, 173–176.
Heineke, C., Hetzel, R., Nilius, N.-P., Zwingmann, H., Todd, A., Mulch, A., Wölfler, A., Glotzbach, C., Akal, C., Dunkl, I., 2019. Detachment faulting in a bivergent core complex constrained by fault gouge dating and low-temperature thermochronology. J. Struct. Geol. 127, 103865.
Hickey, K.A., Barker, S.L.L., Dipple, G.M., Arehart, G.B., Donelick, R.A., 2014. The brevity of hydrothermal fluid flow revealed by thermal halos around giant gold deposits: implications for Carlin-type gold systems. Econ. Geol. 109, 1461–1487.
Hofmann, F., Treffkorn, J., Farley, K.A., 2020. U-loss associated with laser-heating of hematite and goethite in vacuum during (U–Th)/He dating and prevention using high O2 partial pressure. Chem. Geol. 532, 119350.
Huntington, K.W., Klepeis, K.A., 2018. Challenges and Opportunities for Research in Tectonics: Understanding Deformation and the Processes that Link Earth Systems from Geologic Time to Human Time. A Community Vision Document Submitted to the U.S. National Science Foundation: University of Washington, p. 84.
Isambert, A., Valet, J.P., Gloter, A., Guyot, F., 2003. Stable Mn-magnetite derived from Mn-siderite by heating in air. J. Geophys. Res.: Solid Earth 108, 2283.
Ishikawa, T., Tanimizu, M., Nagaishi, K., Matsuoka, J., Tadai, O., Sakaguchi, M., Hirono, T., Mishima, T., Tanikawa, W., Lin, W., 2008. Coseismic fluid–rock interactions at high temperatures in the Chelungpu fault. Nat. Geosci. 1, 679.
Jensen, J.L., Reiners, P.W., Siddoway, C.S., Ault, A.K., Thomson, S.N., Steele-MacInnis, M., 2018. Single-crystal hematite (U-Th)/He dates and fluid inclusions document Cryogenian seismic clastic injection in granite. Earth Planet Sci. Lett. 500, 145–155.
Kameda, J., Ujiie, K., Yamaguchi, A., Kimura, G., 2011. Smectite to chlorite conversion by frictional heating along a subduction thrust. Earth Planet Sci. Lett. 305, 161–170.
Kanamori, H., Riviera, L., 2006. Energy partitioning during an earthquake. In: Abercrombie, R., McGarr, A., Kanamori, H. (Eds.), Earthquakes: Radiated Energy and the Physics of Faulting, Geophysical Monograph Series. American Geophysical Union, Washington, D.C., pp. 3–13
Kirkpatrick, J.D., Rowe, C.D., White, J.C., Brodsky, E.E., 2013. Silica gel formation during fault slip: evidence from the rock record. Geology 41, 1015–1018.
Kuo, L.-W., Song, S.R., Suppe, J., Yeh, E.-C., 2016. Fault mirrors in seismically active fault zones: a fossil of small earthquakes at shallow depths. Geophys. Res. Lett. 43, 1950–1959.
Lachenbruch, A.H., 1986. Simple Models for the Estimation and Measurement of Frictional Heating by an Earthquake: U.S. Geological Survey Open File Report 86-508, p. 13.
Laubach, S.E., Lander, R.H., Criscenti, L.J., Anovitz, L.M., Urai, J.L., Pollyea, R.M., Hooker, J.N., Narr, W., Evans, M.A., Kerisit, S.N., Olsen, J.E., Dewers, T.A., Fisher, D., Bodnar, R., Evans, B.W., Dove, P., Bonnell, L.M., Marder, M.P., Pyrak-Nolte, L., 2019. The role of chemistry in fracture pattern development and opportunities to advance interpretations of geological materials. Rev. Geophys. 57, 1065–1111.
Lindsey, E.O., Fialko, Y., 2013. Geodetic slip rates in the southern San Andreas Fault system: effects of elastic heterogeneity and fault geometry. J. Geophys. Res.: Solid Earth 118, 689–697.
Lippolt, H.J., Brander, T., Mankopf, N.R., 1998. An attempt to determine formation ages of goethites and limonites by (U+th)-^{4}He dating. Neues Jahrbuch fur Mineralogie 11, 505–528.
Lippolt, H.J., Wernicke, R.S., Bahr, R., 1995. Paragenetic specularite and adularia (Elba, Italy): concordant (U+Th)-He and K-Ar ages. Earth Planet Sci. Lett. 132, 43–51.
Loope, D.B., Kettler, R.M., Weber, K.A., 2010. Follow the water: connecting a CO2 reservoir and bleached sandstone to iron-rich concretions in the Navajo Sandstone of south-central Utah, USA. Geology 38, 999–1002.
Louis, S., Luijendijk, E., Dunkl, I., Person, M., 2019. Episodic fluid flow in an active fault. Geology 47, 938–942.
Luders, V., 2016. Contribution of infrared microscopy to studies of fluid inclusions hosted in some opaque ore minerals: possibilities, limitations, and perspectives. Miner. Deposita 91, 1462–1468.
MacNamee, A., Stockli, D.F., 2015. Constraining Age and Locations of Active and Paleofluid Flow Systems in Dixie Valley, Nevada, with Apatite. (U-Th)/He Thermochronometry, AGU Fall Meeting Abstracts, San Francisco, CA. December 2015, abstract # V51H-06.
Magloughlin, J.F., Hall, C.M., van der Pluijm, B.A., 2001. ^{40}Ar-^{39}Ar geochronometry of pseydotachylytes by vacuum encapsulation: North Cascade Mountains, Washington, USA. Geology 29, 51–54.
Maino, M., Casini, L., Ceriani, A., Decarlis, A., Di Giulio, A., Seno, S., Setti, M., Stuart, F. M., 2015. Dating shallow thrusts with zircon (U-Th)/He thermochronometry - the shear heating connection. Geology 43, 495–498.
Mazzarini, F., Musumeci, G., Viola, G., Garofalo, P.S., Mattila, J., 2019. Structural and lithological control on fluid circulation, dilation and ore mineralization (Rio Albano mine, Island of Elba, Italy). J. Struct. Geol. 126, 210–230.
McCalpin, J.P., Nishenko, S.P., 1996. Holocene paleoseismicity, temporal clustering, and probabilities of future large (M > 7) earthquakes on the Wasatch fault zone, Utah. J. Geophys. Res. 101, 6233–6253.
McDermott, R.G., Ault, A.K., Caine, J.S., Reiners, P.W., 2019. Hematite (U-Th)/He constraints on synchronous deformation, hydrothermal alteration, and surface uplift in the eastern Denali ault zone, Yukon, Canada. Geol. Soc. Am. Abstr. Progr. 51 (5). Phoenix, AZ, September 2019.
McDermott, R.G., Ault, A.K., Evans, J.P., Reiners, P.W., 2017. Thermochronometric and textural evidence for seismicity via asperity flash heating on exhumed hematite fault mirrors, Wasatch fault zone, UT, USA. Earth Planet Sci. Lett. 471, 85–93.
McDermott, R.G., Ault, A.K., Wetzel, K.F., 2018. Localization of Seismic and Aseismic Strain in Hematite Vein-Fault Mirror Pairs. AGU Fall Meeting, San Francisco, CA. December 2018, abstract #T11G-0227.
McGarr, A., 1999. On relating apparent stress to the stress causing earthquake fault slip. J. Geophys. Res.: Solid Earth 104, 3003–3011.
McIntosh, R.M., Sharp, J.H., Wilburn, F.W., 1990. The thermal decomposition of dolomite. Thermochim. Acta 165, 281–296.
McNabb, J.C., Dorsey, R.J., Housen, B.A., Dimitroff, C.W., Messé, G.T., 2017. Stratigraphic record of Pliocene-Pleistocene basin evolution and deformation within the southern San Andreas fault zone, Mecca Hills, California. Tectonophysics 719, 66–85.
Miller, H.B.D., Vasconcelos, P.M., Eiler, J.M., Farley, K.A., 2017. A Cenozoic terrestrial paleoclimate record from He dating and stable isotope geochemistry of goethite from Western Australia. Geology 45, 895–898.
Mitchell, T.M., Toy, V., Di Toro, G., Renner, J., Sibson, R.H., 2016. Fault welding by pseudotachylyte formation. Geology 44, 1059–1062.
Monteiro, H., Vasconcelos, P.M., Farley, K.A., Spier, C.A., Mello, C.L., 2014. U-Th)/He geochronology of goethite and the origin and evolution of cangas. Geochem. Cosmochim. Acta 131, 267–289.
Monteiro, H.S., Vasconcelos, P.M.P., Farley, K.A., Lopes, C.A.M., 2018. Age and evolution of diachronous erosion surfaces in the Amazon: combining (U-Th)/He and cosmogenic 3He records. Geochem. Cosmochim. Acta 229, 162–183.
Moore, D.E., Lockner, D.A., 2004. Crystallographic controls on the frictional behavior of dry and water-saturated sheet structure minerals. J. Geophys. Res. Solid Earth 109, B03401. https://doi.org/10.1029/2003JB002582.
Moore, J.C., Roeske, S., Cowan, D.S., Lundberg, N., Gonzales, E., Schoonmaker, J., Lucas, S.E., 1986. Scaly fabrics from deep sea drilling project cores from forearcs. In: Moore, J.C. (Ed.), Structural Fabrics in Deep Sea Drilling Project Cores from Forearcs, GSA Memoir, vol. 166. Geological Society of America, Boulder, CO.
Morales, L.F.G., Lagoeiro, L.E., Endo, I., 2008. Crystallographic fabric development along a folded polycrystalline hematite. J. Struct. Geol. 30, 1218–1228.
Moser, A.C., Evans, J.P., Ault, A.K., Janecke, S.U., Bradbury, K.K., 2017. U-Th)/He thermochronometry reveals Pleistocene punctuated deformation and synkinematic hematite minarlization in the Mecca Hills, southernmost San Andreas Fault zone. Earth Planet Sci. Lett. 476, 87–99.
Murakami, M., Košler, J., Takagi, H., Tagami, T., 2006. Dating pseudotachylyte of the Asuke Shear Zone using zircon fission-track and U–Pb methods. Tectonophysics 424, 99–107.
Murakami, M., Tagami, T., 2004. Dating pseudotachylyte of the Nojima fault using the zircon fission-track method. Geophys. Res. Lett. 31.
Niemeijer, A.R., Di Toro, G., Griffith, W.A., Bistacchi, A., Smith, S.A.F., Nielsen, S.B., 2012. Inferring earthquake physics and chemistry using an integrated field and laboratory approach. J. Struct. Geol. 39, 2–36.
Nuriel, P., Miller, D.M., Schmidt, K.M., Coble, M.A., Maher, K., 2019. Ten-million years of activity within the Eastern California Shear Zone from U–Pb dating of fault-zone opal. Earth Planet Sci. Lett. 521, 37–45.
Nuriel, P., Rosenbaum, G., Uysal, T.I., Zhao, J., Golding, S.D., Weinberger, R., Karabacak, V., Avni, Y., 2011. Formation of fault-related calcite precipitates and their implications for dating fault activity in the East Anatolian and Dead Sea fault zons. Geol. Soc. Lond. Spec. Publ. 359, 229–248.
Nuriel, P., Rosenbaum, G., Zhao, J.-X., Feng, Y., Golding, S.D., Villement, B., Weinberger, R., 2012. U-Th dating of striated fault planes. Geology 40, 647–650.
Nuriel, P., Weinberger, R., Kylander-Clark, A.R.C., Hacker, B.R., Craddock, J.P., 2017. The onset of the Dead Sea transform based on calcite age-strain analyses. Geology 45, 587–590.
Obara, K., Hirose, H., Yamamizu, F., Kasahara, K., 2004. Episodic slow slip events accompanied by non-volcanic tremors in southwest Japan subduction zone. Geophys. Res. Lett. 31, L23602.
Pagel, M., Bonifacie, M., Schneider, D.A., Gautheron, C., Brigaud, B., Calmels, D., Cros, A., Saint-Bezar, B., Landrein, P., Sutcliffe, C., 2018. Improving paleohydrological and diagenetic reconstructions in calcite veins and breccia of a sedimentary basin by combining Δ47 temperature, δ18Owater and U-Pb age. Chem. Geol. 481, 1–17.
Power, W.L., Tullis, T.E., 1989. The relationship between slickenside surfaces in fine-grained quartz and the seismic cycle. J. Struct. Geol. 11, 879–893.
Pozzi, G., De Paola, N., Nielsen, S.B., Holdsworth, R.E., Bowen, L., 2018. A new interpretation for the nature and significance of mirror-like surfaces in experimental carbonate-hosted seismic faults. Geology 46, 583–586.
Proctor, B.P., Mitchell, R.H., Hirth, G., Goldsby, D.L., Zorzi, F., Platt, J.D., Di Toro, G., 2014. Dynamic weakening of serpentinite gouges and bare surfaces at seismic slip rates. J. Geophys. Res. Solid Earth 119, 8107–8131.
Rabinowitz, H.S., Polissar, P.J., Savage, H.M., 2017. Reaction kinetics of alkenone and n-alkane thermal alteration at seismic timescales. G-cubed 18, 204–219.
Reches, Z., Dewers, T.A., 2005. Gouge formation by dynamic pulverization. Earth Planet Sci. Lett. 235, 361–374.

Reiners, P.W., 2005. Zircon (U-Th)/He thermochronometry. Rev. Mineral. Geochem. 58, 151–179.
Reiners, P.W., 2009. Nonmonotonic thermal histories and contrasting kinetics of multiple thermochronometers. Geochem. Cosmochim. Acta 73, 3612–3629.
Reiners, P.W., Chan, M.A., Evenson, N.S., 2014. Radiogenic helium dating and chemistry of diagenetic Fe- and Mn-oxides in Mesozoic sandstones of the Colorado Plateau. Geol. Soc. Am. Bull. 126, 1363–1383.
Rice, J.R., 2006. Heating and weakening of faults during earthquake slip. J. Geophys. Res. 111, B05311.
Riffel, S.B., Vasconcelos, P.M., Carmo, I.O., Farley, K.A., 2016. Goethite (U-Th)/He geochronology and precipitation mechanisms during weathering of basalts. Chem. Geol. 446, 18–32.
Rittner, M., Muller, W., 2011. Dating brittle deformation with the U-Pb method. Geophys. Res. Abstr. 13, EGU2011–13443.
Roberts, N.M.W., Walker, R.J., 2016. U-Pb geochronology of calcite-mineralized faults: absolute timing of rift-related fault events on the northeast Atlantic margin. Geology 44, 531–534.
Rogers, G., Dragert, H., 2003. Episodic tremor and slip on the Cascadia subduction zone: the chatter of silent slip. Science 300, 1942–1943.
Rosière, C.A., Garcia, O.L., Siemes, H., Schaeben, H., 2013. Domainal fabrics of hematite in schistose, shear zone-hosted high-grade Fe ores: the product of the interplay between deformation and mineralization. J. Struct. Geol. 55, 150–166.
Rosière, C.A., Rios, F.J., 2004. The origin of hematite in high-grade iron ores based on infrared microscopy and fluid inclusion studies: the example of the Conceição mine, Quadrilátero Ferrífero, Brazil. Econ. Geol. 99, 611–624.
Rousset, B., Burgmann, R., Campillo, M., 2019. Slow slip events in the roots of the San Andreas fault. Sci. Adv. 5, eaav3274.
Rowe, C.D., Griffith, W.A., 2015. Do faults preserve a record of seismic slip: a second opinion. J. Struct. Geol. 78, 1–26.
Savage, H.M., Brodsky, E.E., 2011. Collateral damage: evolution with displacement of fracture distribution and secondary fault strands in fault damage zones. J. Geophys. Res.: Solid Earth 116.
Savage, H.M., Polissar, P.J., 2019. Biomarker thermal maturity reveals localized temperature rise from paleoseismic slip along the punchbowl fault, CA, USA. G-cubed 20, 3201–3215.
Savage, H.M., Polissar, P.J., Sheppard, R.E., Rowe, C.D., Brodsky, E.E., 2014. Biomarkers heat up during earthquakes: new evidence of seismic slip in the rock record. Geology 42, 99–102.
Scheiber, T., Viola, G., Van der Lelij, R.V., Margreth, A., Schönenberger, J., 2019. Microstructurally-constrained versus bulk fault gouge K-Ar dating. J. Struct. Geol. 127, 103868.
Schleicher, A.M., van der Pluijm, B.A., Warr, L.N., 2010. Nanocoatings of clay and creep of the san Andreas fault at parkfield, California. Geology 38, 667–670.
Scholz, C.H., 2002. The Mechanics of Earthquakes and Faulting. Cambridge University Press, Cambridge, United Kingdom, p. 504.
Sheppard, R.E., Polissar, P.J., Savage, H.M., 2015. Organic thermal maturity as a proxy for frictional fault heating: experimental constraints on methylphenanthrene kinetics at earthquake timescales. Geochem. Cosmochim. Acta 151, 103–116.
Sherlock, S.C., Strachan, R.A., Jones, K.A., 2009. High spatial resolution $^{40}Ar/^{39}Ar$ dating of pseudotachylites: geochronological evidence for multiple phases of faulting within basement gneisses of the Outer Hebrides (UK). J. Geol. Soc. Lond. 166, 1049–1059.
Shuster, D.L., Farley, K.A., 2004. $^{4}He/^{3}He$ thermochronometry. Earth Planet Sci. Lett. 217, 1–17.
Shuster, D.L., Farley, K.A., 2009. The influence of artificial radiation damage and thermal annealing on helium diffusion kinetics in apatite. Geochem. Cosmochim. Acta 73, 183–196.
Shuster, D.L., Farley, K.A., Sisterson, J.M., Burnett, D.S., 2004. Quantifying the diffusion kinetics and spatial distributions of radiogenic ^{4}He in minerals containing proton-induced ^{3}He. Earth Planet Sci. Lett. 217, 19–32.
Shuster, D.L., Farley, K.A., Vasconcelos, P.M., Balco, G., Monteiro, H.S., Waltenberg, K., Stone, J.O., 2012. Cosmogenic ^{3}He in hematite and goethite from Brazilian "canga" duricrust demonstrates the extreme stability of these surfaces. Earth Planet Sci. Lett. 329–330, 41–50.
Shuster, D.L., Flowers, R.M., Farley, K.A., 2006. The influence of natural radiation damage on helium diffusion kinetics in apatite. Earth Planet Sci. Lett. 249, 148–161.
Shuster, D.L., Vasconcelos, P.M., Heim, J.A., Farley, K.A., 2005. Weathering geochronology by (U-Th)/He dating of goethite. Geochem. Cosmochim. Acta 69, 659–673.
Sibson, R.H., 1981. Fluid flow accompanying faulting: field evidence and models. In: Simpson, D.W., Richards, P.G. (Eds.), Earthquake Prediction - an International Review: American Geophysical Union Monograph, vol. 4. Maurice Ewing Series, pp. 593–603.
Siman-Tov, S., Aharonov, E., Boneh, Y., Reches, Z., 2015. Fault mirrors along carbonate faults: formation and destruction during shear experiments. Earth Planet Sci. Lett. 430, 367–376.
Siman-Tov, S., Aharonov, E., Sagy, A., Emmanuel, S., 2013. Nanograins form carbonate fault mirrors. Geology 41, 703–706.
Sleep, N.H., 2019. Thermal weakening of asperity tips on fault planes at high sliding velocities. G-cubed 20, 1164–1188.
Stockli, D.F., Farley, K.A., Dumitru, T.A., 2000. Calibration of the (U-Th)/He thermochronometer on an exhumed fault block, White Mountains, California. Geology 28, 983–986.
Strutt, R.J., 1909. The accumulation of helium in geological time, II. Proc. Roy. Soc. Lond. 83, 96–99.
Stünitz, H., Keulen, N., Hirose, T., Heilbronner, R., 2010. Grain size distribution and microstructures of experimentally sheared granitoid gouge at coseismic slip rates–Criteria to distinguish seismic and aseismic faults? J. Struct. Geol. 32, 59–69.
Sylvester, A.G., Smith, R.R., 1976. Tectonic transpression and basement-controlled deformation in san Andreas fault zone, Salton trough, California. AAPG (Am. Assoc. Pet. Geol.) Bull. 60, 2081–2102.
Tagami, T., 2005. Zircon fission-track thermochronology and applications to fault studies. Rev. Mineral. Geochem. 58, 95–122.
Tagami, T., 2012. Thermochronological investigations of fault zones. Tectonophysics 538–540, 67–85.
Tagami, T., 2019. Application of Fission-Track Thermochronology to Understand Fault Zones, Fission-Track Thermochronology and its Application to Geology. Springer, pp. 221–233.
Tagami, T., Murakami, T., 2007. Probing fault zone heterogeneity on the Nojima fault: constraints from zircon fission-track analysis of borefole samples. Tectonophysics 443, 139–152.
Tarling, M.S., Rowe, C.D., 2016. Experimental slip distribution in lentils as an analog for scaly clay fabrics. Geology 44, 183–186.
Taylor, M.P., Ault, A.K., Newell, D.N., 2019. Hematite microtextures and (U-Th)/He thermochronometry of the Hurricane fault, southwestern Utah: evidence for a paleoearthquake? Geol. Soc. Am. Abstr. Progr. 51 (5). Phoenix, AZ, September 2019.
Tenthorey, E., Cox, S.F., Todd, H.F., 2003. Evolution of strength recovery and permeability during fluid–rock reaction in experimental fault zones. Earth Planet Sci. Lett. 206, 161–172.
Uysal, T.I., Feng, Y., Zhao, J.-X., Altunel, E., Weatherley, D., Karabacak, V., Cengiz, O., Golding, S.D., Lawrence, M.G., Collerson, K.D., 2007. U-series dating and geochemical tracing of late Quaternary travertine in co-seismic fissures. Earth Planet Sci. Lett. 257, 450–462.
van der Pluijm, B.A., Hall, C.M., Vrolijk, P.J., Pevear, D.R., Covey, M.C., 2001. The dating of shallow faults in the Earth's crust. Nature 412, 172–175.
Vannucchi, P., 2019. Scaly fabric and slip within fault zones. Geosphere 15, 342–356.
Vannucchi, P., Maltman, A., Bettelli, G., Clennell, B., 2003. On the nature of scaly fabric and scaly clay. J. Struct. Geol. 25, 673–688.
Vasconcelos, P.M., Heim, J.A., Farley, K.A., Monteiro, H., Waltenberg, K., 2013. $^{40}Ar/^{39}Ar$ and (U-Th)/He - $^{4}He/^{3}He$ geochronology of landscape evolution and channel iron deposits genesis at Lynn Peak, Western Australia. Geochem. Cosmochim. Acta 117, 283–312.
Verberne, B.A., Spiers, C.J., Niemeijer, A.R., de Bresser, J.H.P., de Winter, D.A.M., Plumper, O., 2013. Frictional properties and microstructure of calcite-rich fault gouges sheared at sub-seismic sliding velocities. Pure Appl. Geophys. 171, 2617–2640.
Verhaert, G., Muchez, P., Sintubin, M., Similox-Tohon, D., Vandycke, S., Waelkens, M., 2003. Reconstruction of neotectonic activity using carbonate precipitates: a case study from northwestern extremity of the Isparta Angle (SW Turkey). J. Geochem. Explor. 78–79, 197–201.
Vrolijk, P.J., van der Pluijm, B.A., 1999. Clay gouge. J. Struct. Geol. 21, 1039–1048.
Watanabe, Y., Nakai, S.I., Lin, A., 2008. Attempt to determine U-Th ages of calcite veins in the Nojima fault zone, Japan. Geochem. J. 42, 507–513.
Wells, M.L., Snee, L.W., Blythe, A.E., 2000. Dating of major normal fault systems using thermochronology: an example from the Raft River detachment, Basin and Range, western United States. J. Geophys. Res.: Solid Earth 105, 16303–16327.
Wernicke, R.S., Lippolt, H.J., 1993. Botryoidal hematite from the Schwarzwald (Germany): heterogeneous uranium distributions and their bearing on the helium dating method. Earth Planet Sci. Lett. 114, 287–300.
Wernicke, R.S., Lippolt, H.J., 1994a. ^{4}He age discordance and release behavior of a double shell botryoidal hematite from the Schwarzwald, Germany. Geochem. Cosmochim. Acta 58, 421–429.
Wernicke, R.S., Lippolt, H.J., 1994b. Dating of vein specularite using internal (U+Th)/^{4}He isochrons. Geophys. Res. Lett. 21, 345–347.
Wernicke, R.S., Lippolt, H.J., 1997. U+Th)-He evidence of Jurassic continuous hydrothermal activity in the Schwarzwald basement, Germany. Chem. Geol. 138, 273–285.
Wolf, R.A., Farley, K.A., Silver, L.T., 1996. Helium diffusion and low temperature thermochronometry of apatite. Geochem. Cosmochim. Acta 60, 4231–4240.
Wolfler, A., Kurz, W., Danisik, M., Rabitsch, R., 2010. Dating of fault zone activity by apatite fission track and apatite (U-Th)/He thermochronometry: a case study from the Lavanttal fault system (Eastern Alps). Terra. Nova 22, 274–282.
Yapp, C.J., Shuster, D.L., 2011. Environmental memory and a possible seasonal bias in the stable isotope composition of (U-Th)/He-dated goethite from the Canadian Arctic. Geochem. Cosmochim. Acta 75, 4194–4215.
Zeitler, P.K., Herczig, A.L., McDougall, I., Honda, M., 1987. U-Th-He dating of apatite: a potential thermochronometer. Geochem. Cosmochim. Acta 51, 2865–2868.
Zwingmann, H., Mancktelow, N., 2004. Timing of Alpine fault gouges. Earth Planet Sci. Lett. 223, 415–425.